SET-UP AND EVALUATION OF A MID-INFRARED REFLECTOMETER AND INVESTIGATION OF THE OPTICAL PROPERTIES OF DOPED TIN TELLURIDE ALLOYS

By

Halima Hawesa

B. Sc. (Physics) 7TH APRIL UNIVERSITY, ZAWIA, LIBYA

A THESIS SUBMITTED IN PARTIAL FULFILLMENT OF

THE REQUIREMENTS FOR THE DEGREE OF

MASTER OF SCIENCE

in

THE FACULTY OF MATHEMATICS AND SCIENCE

DEPARTMENT OF PHYSICS

We accept this thesis as conforming

to the required standard

.....

.....

.....

.....

BROCK UNIVERSITY

JUNE 1998

In presenting this thesis in partial fulfilment of the requirements for an advanced degree at Brock University, I agree that the Library shall make it freely available for reference and study. I further agree that permission for extensive copying of this thesis for scholarly purposes may be granted by the head of my department or by his or her representatives. It is understood that copying or publication of this thesis for financial gain shall not be allowed without my written permission.

Department of PHYSICS
Brock University
500 Glenridge Avenue
St. Catharines, Ontario
Canada L2S 3A1

Date:

Abstract

A system comprised of a Bomem interferometer and a LT3-110 Heli-Tran cryostat was set up to measure the reflectance of materials in the mid-infrared spectral region. Several tests were conducted to ensure the consistency and reliability of the system. Silicon and Chromium, two materials with well known optical properties were measured to test the accuracy of the system, and the results were found to be in good agreement with the literature.

Reflectance measurements on pure SnTe and several Pb and Mn-doped alloys were carried out. These materials were chosen because they exhibit a strong plasma edge in the mid infrared region. The optical conductivity and several related optical parameters were calculated from the measured reflectance. Very low temperature measurements were carried out in the far-infrared on $Sn_{98}Mn_2Te$, and the results are indicative of a spin glass phase at 0.8 K.

Resistivity measurements were made at room temperature. The resistivity values were found, as expected, to decrease with increasing carrier concentration and to increase with increasing manganese concentration.

Table of Contents

List of Tables

List of Figures

Acknowledgement

I would first like to thank the Libyan Government for giving me the chance to study abroad. My work here would not have been possible without their financial support and trust.

I thank Dr. W. H. Cade, Dean, Faculty of Mathematics and Science, Dr. F. S. Razavi, Chair of the Physics Department, and Dr. M. Reedyk, Supervisor, for offering me this position for completing a MSc degree at Brock University.

I am grateful to Dr. R. Shukla for his encouragement and for answering all my questions from any field in physics. I appreciated the help I received from the people working in the Machine shop and the Electronic shop, when I needed it for my lab project.

To Alice Witvoet, for her patience and support, a warm thank you. I also thank Cathy Butera for her constant friendship. A good luck wish to my office mates, Mylo Hildebrand and Rodica Ellison. To the members of the muslim community in St. Catharines a heartfelt thank you for welcoming me and making me feel at home. Thanks to the people in CBIE, for their cooperation and fine services, which made my life in Canada much easier.

Finally, a deep thank you to my family for their love and support that made everything possible, and to all my friends and my husband, Mohamad, for being there for me all the time.

Chapter 1

Introduction

Reflection spectroscopy is widely used in the study of solids, particularly in determining optical constants [1].

The infrared region of the electromagnetic spectrum, shown in Figure 1.1, is subdivided into three regions: the near infrared, the mid infrared, and the far infrared. There are variations in the instrumentation employed within each subdivision, and also differences in the information typically obtained from each region [1, and 2].

The region from 0 to 400 cm^{-1} of the electromagnetic spectrum is called the far infrared. Solids show many characteristic excitations in this region such as free carrier absorption, magnons and phonons. The mid infrared covers the region from 400 to 6000 cm^{-1}. The majority of molecular vibrations of chemical significance occur in this region, as do interband transitions and strong bound carrier absorption, which provides information about the band structure of materials. The near infrared and visible-ultraviolet of the spectrum regions cover frequencies from 6000 cm^{-1} to 13000 cm^{-1} and from 13000 cm^{-1} to 40000 cm^{-1}, respectively.

During the course of this thesis work a system comprised of a Bomem interferometer, and a Helium-4 cryostat, was setup to measure the reflectance of a single crystal samples

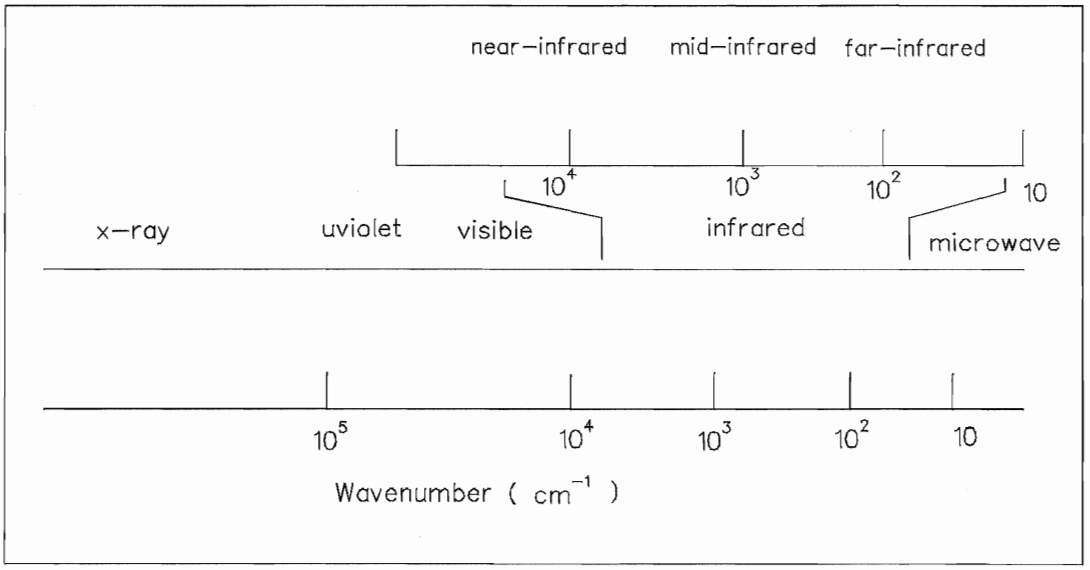

Figure 1.1: The electromagnetic spectrum.

in the mid-infrared spectral region. The system was evaluated and then tested by measuring the absolute reflectance of Chromium and Silicon, two materials with well known optical properties. This is the subject of Chapters 2 and 3. The system was then used to undertake a study of the optical properties of SnTe and several Pb/Mn-doped alloys which is presented in Chapter 5. The reflectance measurements at 300 K were extended to 30000 cm^{-1} using a Grating spectrometer to facilitate Kramers-Kronig analysis in order to obtain the optical constants.

Previous studies showed that Mn-doped Tin Telluride alloys may experience a transition to a spin glass state at very low temperatures, depending on the free carrier concentration, and the concentration of magnetic Manganese ions [3, 4, and 5]. Thus, to complete the study of the optical properties of this system, the reflectance of $Sn_{98}Mn_2Te$, which is of a composition expected to show spin glass behaviour, was investigated in the

far infrared at temperatures as low as 0.8 K using a Helium-3 cryostat and Martin-Pupplett type polarizing interferometer. The results are presented in Chapter 6.

Chapter 2

System Apparatus

2.1 Introduction

This chapter will describe the components that comprise a system setup at Brock University during the course of this thesis work to measure the absolute mid-infrared reflectance at temperatures ranging from 10 K to 325 K using an in-situ evaporation technique first described by Homes [6].

2.2 General view

The mid-infrared system is shown in Figures 2.1(a) and (b) and consists of a Bomem Michelson Interferometer, a Heli-Tran model Lt3-110 cryostat [7], a set of mirrors to redirect the light to the cryostat and back to the detector, and an Evaporator. Figure 2.1(a) illustrates schematically the main components of the system including the light path direction, while Figure 2.1(b) gives a general overview of the system.

2.3 System Specifications

2.3.1 Bomem Interferometer

The Bomem interferometer is an optical instrument, of dimensions $47 \times 35 \times 14$ cm^3 consisting of a sample compartment and a sealed interferometer compartment.

The sample compartment is enclosed in a purge cover provided with an access door.

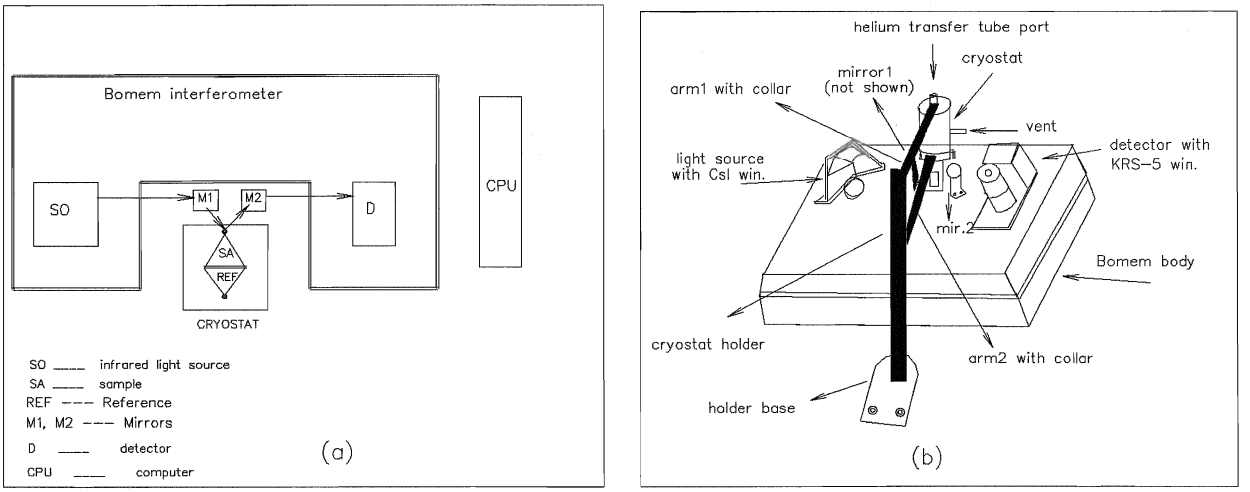

Figure 2.1: Components comprising the mid-infrared system. (a) Schematic showing main components. Arrows show the light path. (b) General overview.

It contains a set of mirrors to channel infrared radiation from the light source to the detector, a model D11X type MCT for the range 500 -6000 cm^{-1} with an active element of size 1 mm^2. The system was originally provided with a sample holder, for transmission measurements, shown in Figure 2.2 which is mounted on a kinematic plate placed between the source and the detector. For reflectance measurements this kinematic plate is replaced with an identical plate on which are mounted the two mirrors used to redirect the light beam to the cryostat and back to the detector. This allows one to readily switch between transmission and reflectance modes.

The purge cover can be lifted or removed to install large accessories. For the system described herein the cover has been lifted to install the cryostat.

The sealed interferometer compartment contains a Globar mid-infrared light source for the range 200 - 6500 cm^{-1} , a Michelson interferometer with an infrared-transmitting

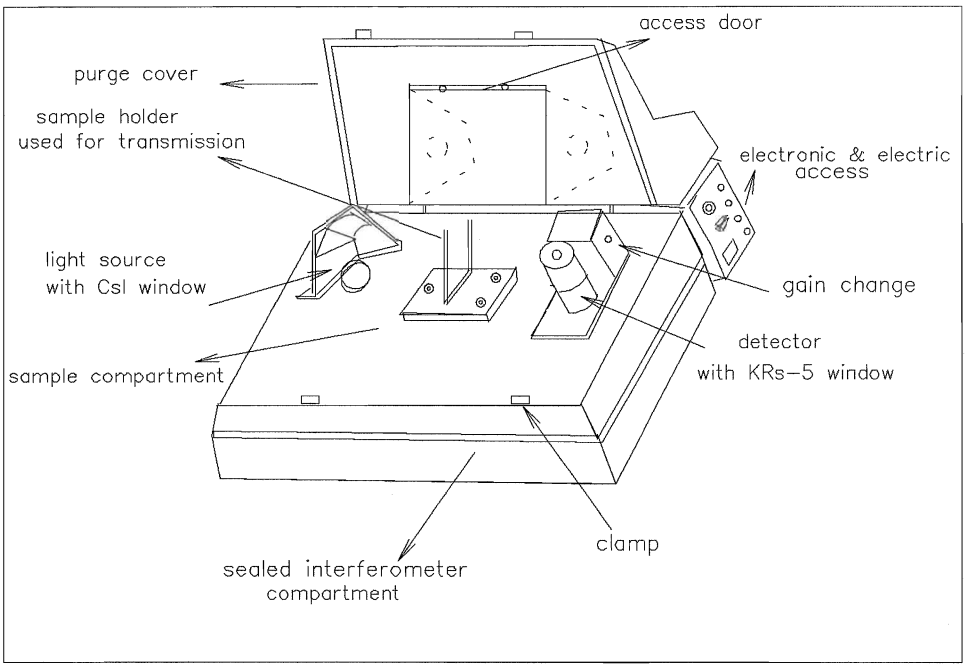

Figure 2.2: The Bomem Interferometer overview. The top cover is lifted in order that the cryostat may be installed. The CsI window is protected with a plastic cap containing a desiccant to absorb moisture from the air when the interferometer is not in use.

CsI beamsplitter, a Helium-Neon laser for the measurement of scan position, and various power supplies and electronic assemblies. The cast aluminum compartment is sealed to prevent the entry of dust and moist air, which can damage and cause drift in the beam-splitter.[8]

Figure 2.3 illustrates the principles of operation of the Bomem interferometer. The beam from the light source is first collimated and then travels to the beamsplitter, which passes half of the light to a fixed mirror and reflects the other half to a moving mirror. The two beams are then reflected back from the mirrors, recombined and focussed on the detector by a series of mirrors. The difference in length of the two paths gives rise to an interference pattern known as an interferogram. The interferogram is then fast Fourier transformed (FFT) to give a spectrum of intensity as a function of wavenumber.

The software used to collect the interferogram, perform the Fourier transform, and to do basic data manipulation was provided by the Bomem Hartmann and Braun Company.

2.3.2 Heli-Tran model LT-3-110 Cryostat

The cryostat provides refrigeration to cool the sample from 300 to 10 K. It is made of non-magnetic stainless steel and consists of three main parts. The heart of the cryostat is a copper tube of 12.5 mm outer diameter, referred to as the cold finger. It is sealed at the cold tip end and threaded in order to connect a sample holder. A transfer tube can be inserted to cool the sample to $\sim$ 10 K using liquid helium. For temperatures above 77 K, it was found to be more convenient to use liquid nitrogen, which can be poured directly into the cold finger using a funnel.

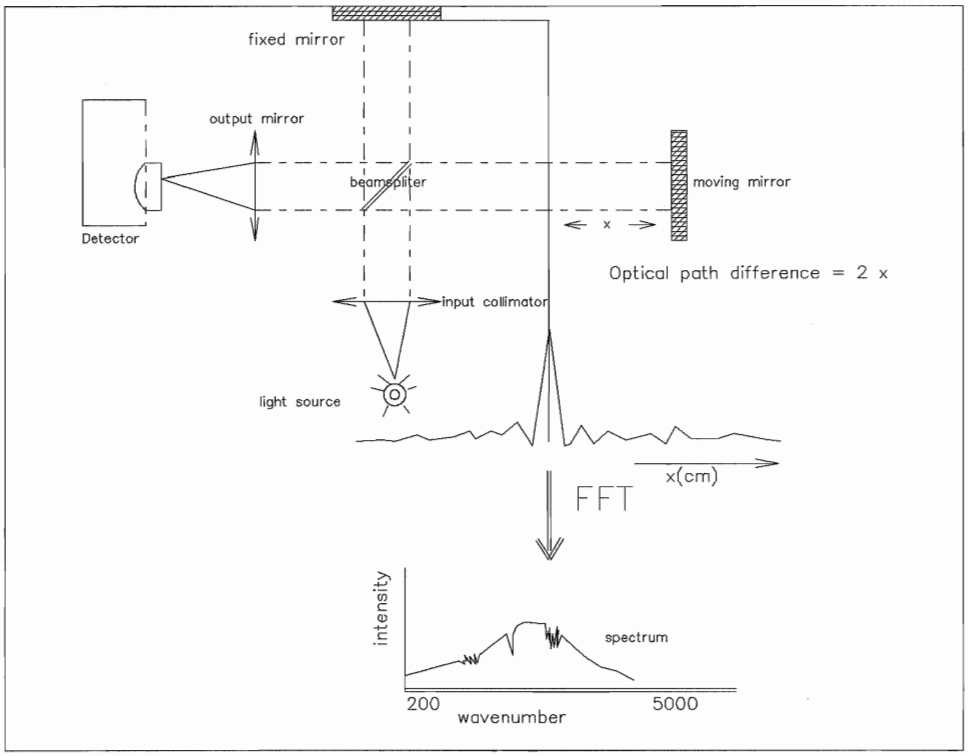

Figure 2.3: The principle of operation of the Bomem Interferometer. The light coming from the light source is collimated and directed to the beam-splitter which passes half of the light to the fixed mirror, and reflects the other half to the moving mirror. The two beams then reflect back from the mirrors, recombine and are focussed by a series of output mirrors on the detector. By applying an FFT, the resulting interferogram is converted to a spectrum.

A Chromel and gold with 0.07 atomic % iron thermocouple is mounted in the cold tip to track the sample temperature. Outside the cryostat these wires are connected to copper wires and the junctions are sealed using epoxy in a glass tube filled with oil. The ends of the copper wires protrude from the tube in order to connect a voltmeter. The glass tube is placed in an ice bath reference while it is in use. The sample temperature is determined by adding the thermocouple output reading (in mV) to 5.266 mV which is the thermal voltage corresponding to an ice reference (273 K), and noting the corresponding temperature in Table III-2 of reference [7].

The cold finger also houses a set of heater wires, which upon application of $\sim$ 16 V using an external power supply can bring the sample up to room temperature from liquid Nitrogen temperature in approximately 30 minutes.

The outer stainless steel jacket is kept from freezing at room temperature while cooling down the cryostat by passing a current through the shield heater. When the cryostat is being used with Helium the gas outlet port on the main body is connected to a flow meter in order to control the helium flow rate. Figure 2.4 shows an overview of the helium transfer operation.

The sample holder, made of copper and brass is screwed into the end of the cold tip.

A stainless steel radiation shield which exposes the reference and sample via small openings can be used to enclose the cold finger, thereby allowing one to reach lower temperatures.

The lower body is essentially a vacuum shroud, which encloses the cold finger via double O-ring seals on the main body. It has two flanges on the front and back sides and

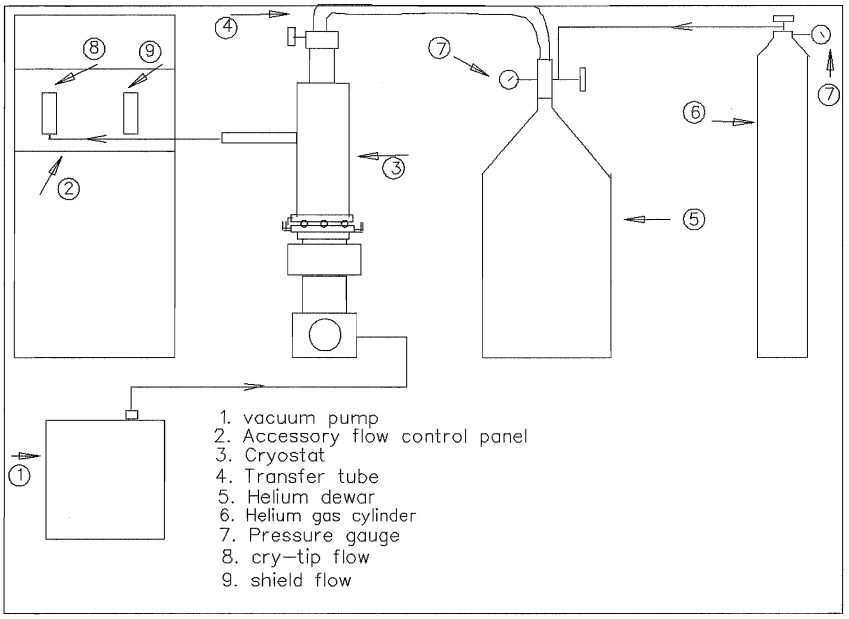

Figure 2.4: Helium transfer operation. Helium is transferred to the cryostat by pressurizing the helium dewar with Helium gas. The flow rate can be controlled via a flow meter.

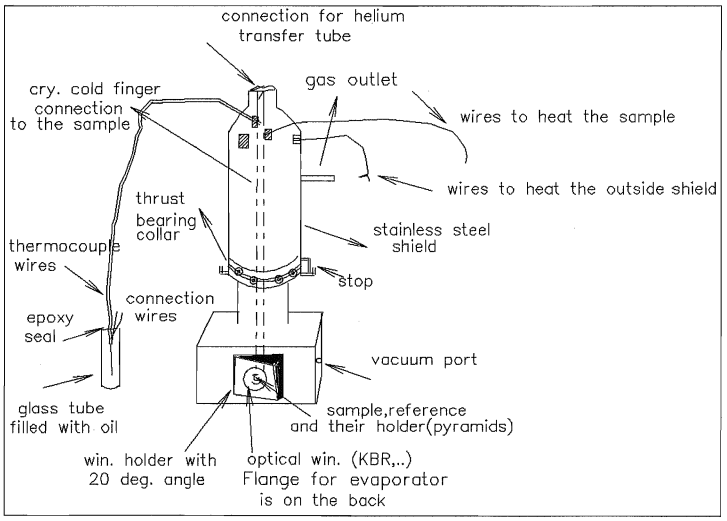

Figure 2.5: Cryostat body and connections to the outside.

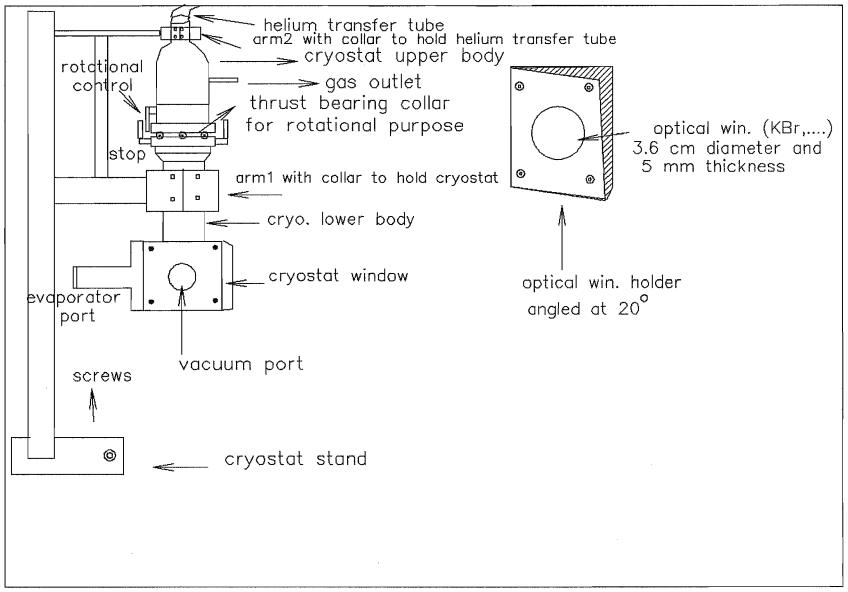

Figure 2.6: Cryostat and stand, side view.

a port for a vacuum connection. The front flange of the lower body contains an optical window (KBr, CsI, or NaCl) mounted in an Aluminum holder at a 20° angle in order to direct window reflections away from the detector. An evaporator used for in-situ gold evaporation is attached to the rear flange of the lower body.

Figure 2.5 shows the main LT3-110 Heli-Tran connections, while Figure 2.6 gives a side view of the cryostat and its holder. As shown in Figure 2.6, a thrust bearing has been attached to the lower body of the cryostat by way of a collar. Two adjustable screws are attached to opposite sides of the collar to work as stops when reversing 180° between the sample and the reference. A matching collar connected to the main body, has a protruding "finger" which comes to rest on the stops. The cryostat is held in place by tightening the lower collar of the stand around the cryostat's lower body. The upper collar of the stand is used to support the helium transfer tube. In this way one

is able to rotate the main body of the cryostat 180° to switch between the sample and the reference without moving the lower body of the cryostat. Several adjustments are possible on the thrust bearing collars to ensure a smooth, level rotation.

2.3.3 Sample Holder

The sample holder is comprised of several pieces, including two highly polished brass pyramids, designed with a 2 cm diameter base at a 20° angle. The pyramids have three threaded holes which are used to attach them to a mounting plate. The angle of the pyramids can be adjusted by three set screws which go through the plates.

The sample and the reference are attached to the tips of the pyramids using five minute epoxy. This bonding medium was chosen because it is soluable in hot acetone, and therefore samples can be easily removed from, and reattached to the pyramid. The two copper mounting plates, which are 2 cm in diameter and 5 mm thick, are attached with 0-80 screws to a copper plate which is mounted on a threaded rod which can be screwed into the cold tip of the cryostat. The sample holder was designed in this pyramid shape to direct all reflected light away from the detector except that coming from the sample. Figure 2.7 shows the pieces comprising the sample holder.

2.3.4 The Evaporator

The Evaporator, shown in figure 2.8, is constructed of two stainless steel rods of 10.5 cm length and 3.2 mm diameter. Each rod has a 0-80 hole tapped on each end. The rods are epoxied into ceramic beads which in turn are epoxied into a vacuum flange. The exterior ends of the rods are connected to wire leads with 0-80 screws. A tungsten coil filament is attached across the interior ends. The tungsten wire used has a diameter of 0.02 mm. For evaporation purposes, three small gold rings are attached to the tungsten

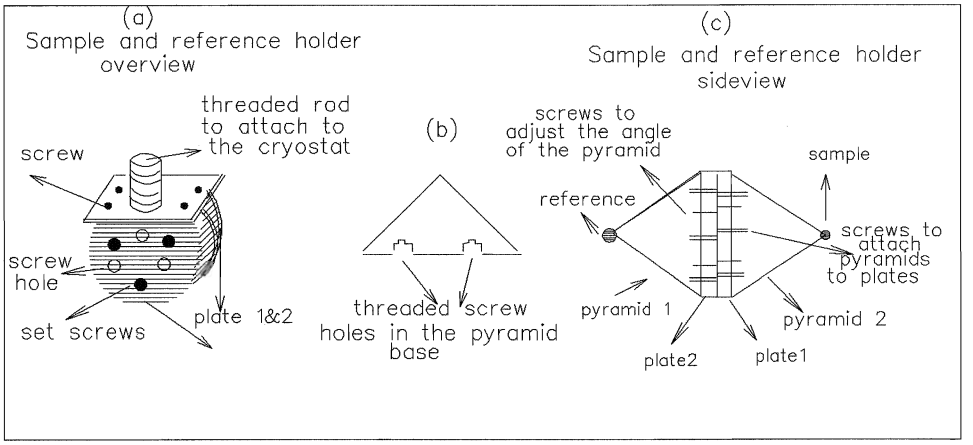

Figure 2.7: The sample holder design.

filament. The gold wire used to make the rings has a diameter of 0.25 mm. Each ring is made of a piece of wire of 6 mm approximate length.

The evaporator flange is attached via an O-ring and locking clamp to a cylindrical brass shield of 2.11 cm diameter and 9 cm length which is welded to a plate which attaches to the rear flange of the lower body of the cryostat. For evaporation, the system is evacuated to a pressure of $\approx 10^{-6}$ Torr, the sample is placed such that it faces the filament, the circuit is connected as shown in Figure 2.8, and a 2 A current is passed through the tungsten filament for 20 seconds.

2.3.5 Optical Windows

In the mid-infrared, alkali-halide materials such as NaCl, KBr and CsI can be used for optical windows. Discs of NaCl and KBr, 3 cm in diameter and 6.88 mm in thickness, were purchased for this purpose. Because the cryostat window holder was designed to accommodate windows with a depth of 5 mm, the discs were polished down to this

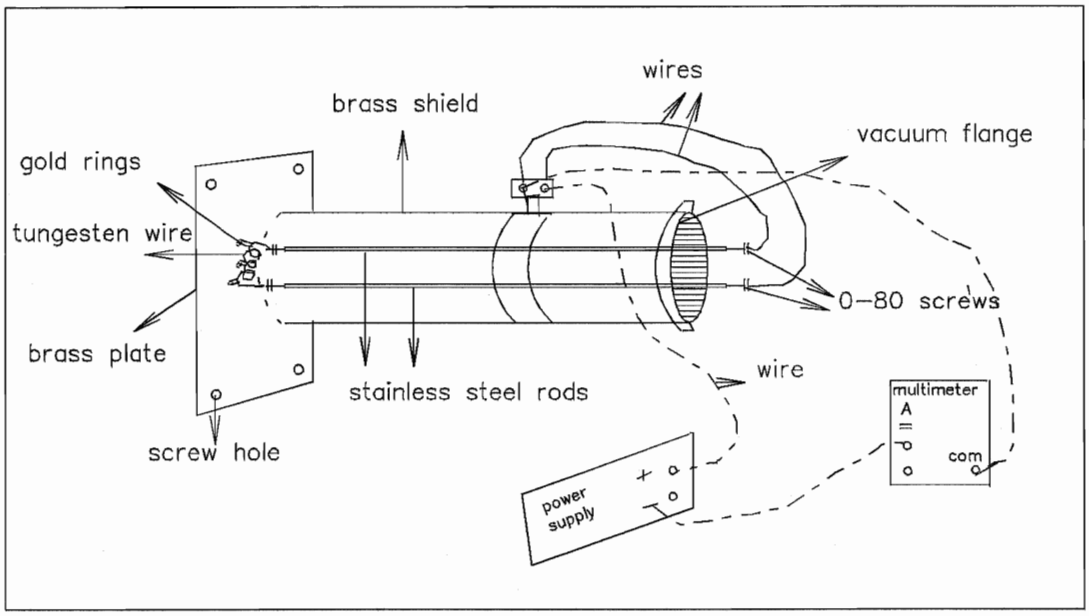

Figure 2.8: The Evaporator design and circuit used.

thickness; first using 400 and 600 emory paper followed by a rouge paste (iron oxide) on a lapping cloth. A KBr window was used for the experiments discussed in the following chapters. The transmission of the optical windows, measured using the Bomem interferometer, is given in appendix A.

2.3.6 Cryostat Stand

The cryostat stand, shown in Figures 2.1 and 2.6, is screwed to the table on which the Bomem interferometer sits, and can be used to adjust the height of the cryostat. It has two arms whose height can be adjusted by way of a sliding mechanism. Each arm ends in a collar. The upper collar is moveable and is used to hold the Helium transfer tube. The lower collar is used to hold the lower body of the cryostat.

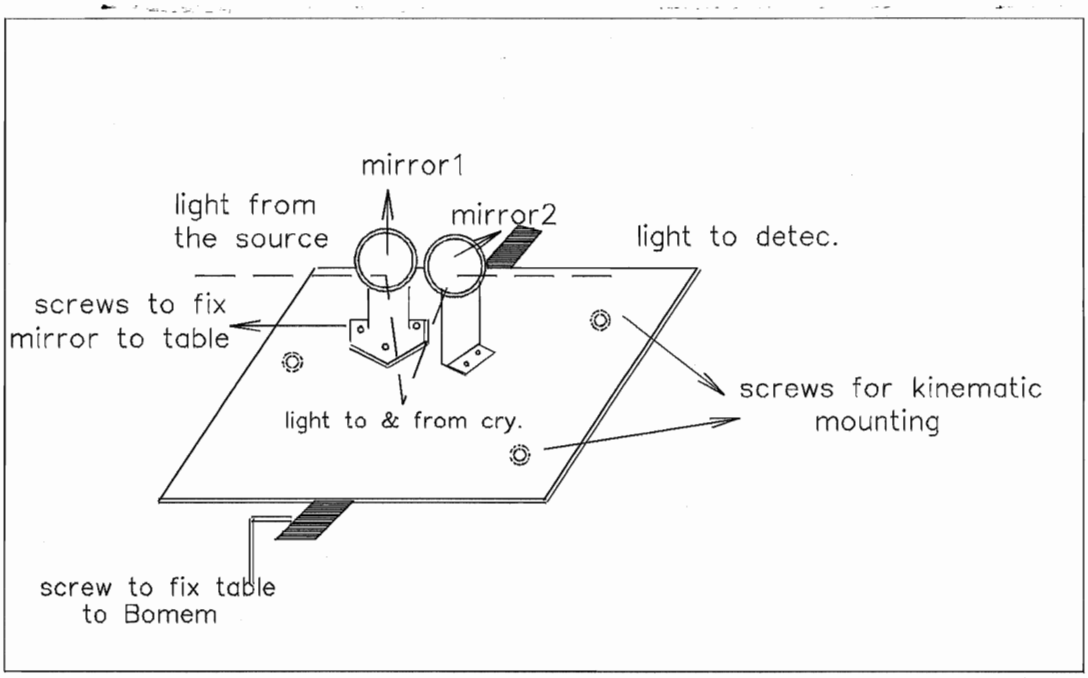

Figure 2.9: The Mirror holder. Dashed lines show the light path.

2.3.7 Deflecting Mirrors

Two spherical mirrors, one 8 cm in diameter, the other 6 cm in diameter, were arranged, as shown in Figure 2.9, on a kinematically mounted table of dimensions $5.5 \times 12 \times 0.63$ cm^3, in order to deflect the light from the Bomem to the cryostat and back from the cryostat to the detector. The angle of incidence for the sample is about 15°. The table is fixed to the Bomem by a set of screws. The entire table can be easily removed to switch the Bomem from reflectance to transmission mode, shown in Figure 2.2.

Chapter 3

Evaluating the System

3.1 Introduction

Before a system can be used to investigate samples with unknown optical properties it must be evaluated for accuracy and reliability. This is the focus of this chapter. Sections 3.2 and 3.3 discuss two tests performed to evaluate the reproducibility and reliability of the system, while sections 3.4 and 3.5 give the results of reflectance measurements of silicon and chromium, materials with well known optical properties, in order to determine the accuracy.

3.2 100% line

The 100% line for a system yields a measure of its consistency. In particular it evaluates the stability of the system with regard to sample/reference repositioning.

In order to measure the 100% line for the system, a small Aluminum mirror, 6.1 mm in diameter and 0.7 mm thick, was glued to one of the pyramids, and used as a sample, while the other pyramid was left bare. A spectrum was collected from the mirror. The upper cryostat was then rotated through 180° to the bare pyramid and back again to the mirror. A second spectrum was then collected. The two spectra were divided, yielding the 100% line for the system. Ideally the ratio will equal 1.0 (ie. 100%) for all frequencies. That is, one expects a horizontal line located at 1.0.

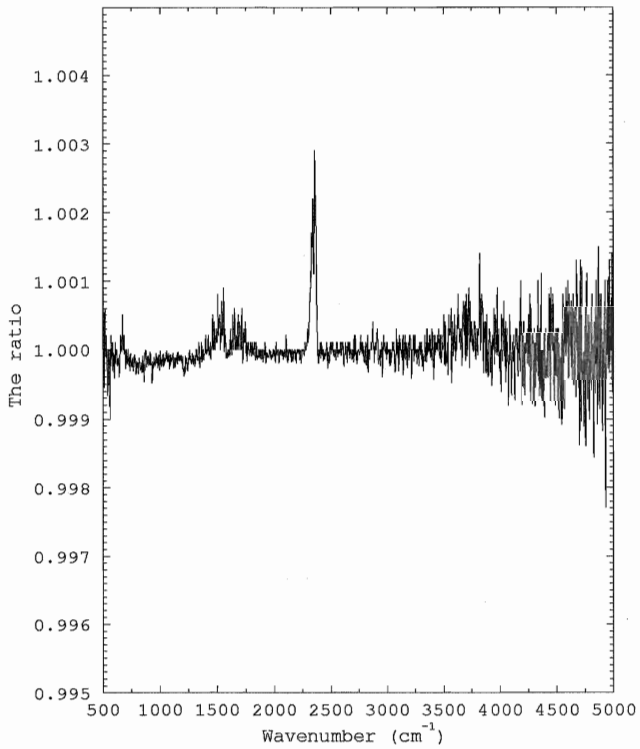

Figure 3.1: The 100% line of the system shown as a ratio on an expanded scale which has a total span of 1% .

The procedure was repeated 15 times, and an average calculated. The result is shown in Fig 3.1, and confirms that the system has excellent reproducibility. The scatter in the data gives an indication of the signal to noise capability of the system. Under the conditions described above one can see from Fig 3.1 that between 750 and 3500 cm^{-1} the peak-to-peak noise has an average value of 0.07 of a percent. It increases beyond 3000 cm^{-1}, reaching a peak-to-peak value of approximate 0.2%, at 5000 cm^{-1}. The MCT detector cuts out near 500 cm^{-1}, which gives rise to the increased noise level below 750 cm^{-1}. Isolated spurious peaks and regions of increased noise between 750 cm^{-1} and 3000 cm^{-1} are due to regions with significant absorption structure from air in the power spectrum.

3.3 Leakage signal

To eliminate reflections from the cryostat window and its holder from reaching the detector, the holder was designed such that the window is mounted at a 20° angle. Furthermore the front face was covered by a special radiation-absorbing foam. The sample holder itself was designed as a conical pyramid to scatter light reflected from it out of the path to the detector. The final step was to evaluate the extent of any remaining 'leakage' signal, which can be defined as a signal arising due to any reflections but those from the sample. The leakage signal was measured with the same mirror used in the 100% line test. The procedure was to collect a spectrum first from the mirror and then from the bare pyramid. The leakage signal is then calculated according to:

$$leakage\ signal = \frac{spectrum\ from\ bare\ pyramid}{spectrum\ from\ pyramid\ with\ sample}. \tag{3.1}$$

Ideally, the leakage signal is expected to be a horizontal line located at zero. As shown in Fig 3.2, the leakage signal for this system is a little over a tenth of a percent for the full spectral range, which seems acceptable. This method of evaluating the leakage

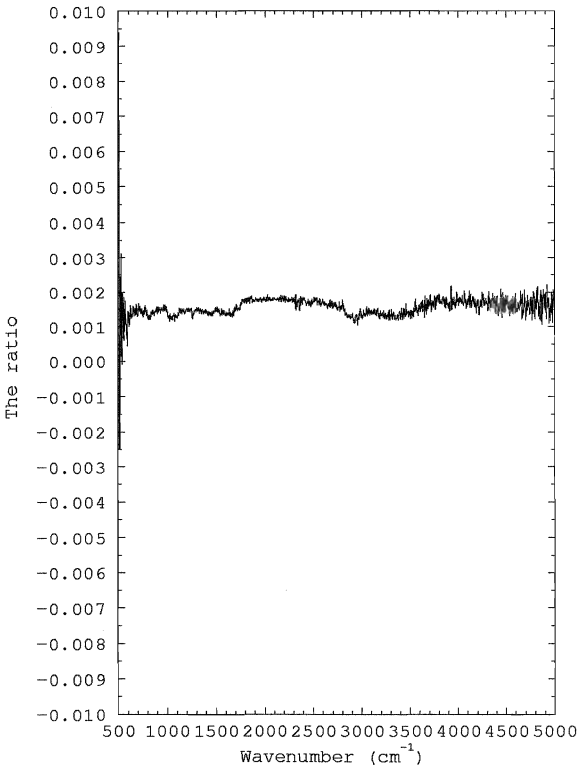

Figure 3.2: The Leakage signal of the system measured under the conditions described in the text.

signal of course depends on the size of the mirror. Its significance becomes greater as the samples become smaller.

Because the infrared beam is not visible it is not easy to determine from where any leakage arises. In addition to the cryostat window and its holder, it could arise from the outside of the cryostat, from the sample holder, or from the inside walls of the cryostat. As a further test, the inside walls of the cryostat were covered with absorption foam however no significant difference in the leakage signal was observed.

3.4 The Reflectance of Silicon

Silicon, a material with extremely well-known optical properties, was measured to test the accuracy of the mid-infrared system. Silicon is a semiconductor with a metallic appearance at visible wavelengths, and a band gap at 1.1 eV which lies in the infrared [9]. The absorption spectrum rises rapidly above 3 eV with a maximum near 3.5 eV related to the onset of a strong direct optical transition [10]. A number of investigators have measured the optical properties of silicon in the near and far infrared regions, using different measuring techniques as reported in Palik [11].

3.4.1 Experimental Details

Two samples of highly polished, high purity Silicon of dimensions ($3.5 \times 3.3 \times 0.6$) mm^3 and ($2.6 \times 5 \times 0.6$) mm^3 were measured. An Aluminum mirror, of 6.1 mm diameter was used as reference.

For each experiment, the sample and the reference were attached to the pyramids with 5 minute epoxy. In order to ensure that the sample and the reference were mounted in a position parallel to the pyramid base a mounting device, shown in Figure 3.3, was used.

After mounting the sample and the reference, and preparing the evaporator filament, the cryostat was evacuated to a vacuum of the order 10^{-6} Torr. After cooling the detector with liquid Nitrogen, data was collected at room temperature, alternating between the sample and the reference until typically 30 ratios of sample to reference spectra were obtained and averaged to improve signal to noise. A gold overlayer was then deposited on the sample at room temperature by passing a current of 2 A through the evaporator filament, located 2 cm from the sample, for twenty seconds. Ratios of the gold-coated

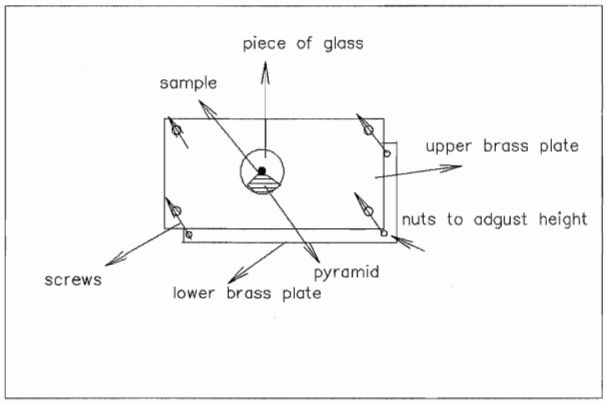

Figure 3.3: The sample mounting device.

sample spectrum to that of the unaffected reference were then collected and averaged. The final reflectance was determined by dividing the first ratio by the ratio for the gold coated sample:

$$Reflectance = \frac{\frac{sample}{reference}}{\frac{coated\,sample}{reference}}. \tag{3.2}$$

The reference essentially cancels out in this procedure. It is used to eliminate the effects of drift in the intensity of the light source and in the detector sensitivity which might occur over the course of data collection. The final absolute reflectance is obtained by multiplying by 0.985, which is the reflectance of gold in the investigated region [11]. The results for the two samples are shown in Figure 3.4, along with a comparison to literature values.[11]

The results obtained by this system show reasonable agreement with the literature data which is lower by about 2%, this difference might arise from differences in sample preparation but is more likely due to reflections from the back surface of the sample. Note that the reflectance of the two samples measured is in good agreement, except in the region ≤ 550 cm^{-1} which is near where the detector cuts out.

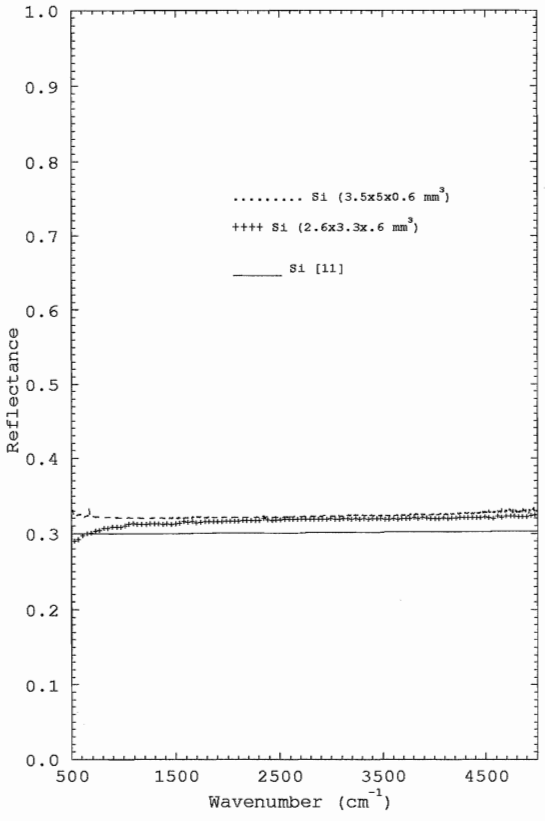

Figure 3.4: Silicon reflectance measured with this system along with a comparison to literature values from Palik[11].

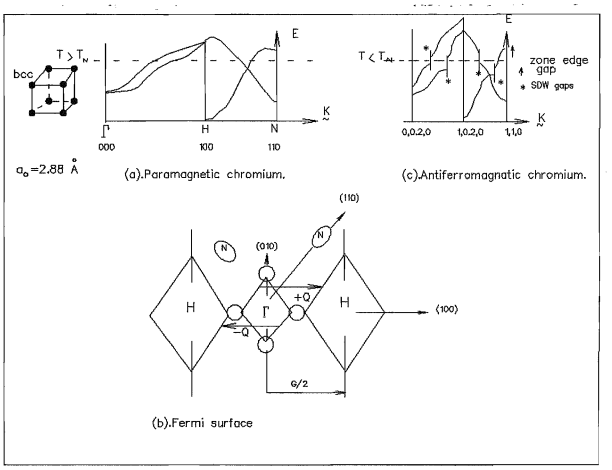

Figure 3.5: The energy bands for chromium, where (a) shows a unit cell and the band structure of paramagnetic chromium. The Fermi energy is drawn as a dashed line. (b) shows the Fermi surface of paramagnetic chromium derived from the bands. Nesting between the octahedral surfaces for the electrons and holes centered at Γ and H respectively, causes the opening of a SDW gap in the band structure of antiferromagnetic chromium shown in (c). The figure is after [14] and [20].

3.5 The Reflectance of Chromium

3.5.1 Introduction

Chromium is an antiferromagnet with a Nèel temperature of , $T_N = 312K$. The magnetic ordering is not however exactly commensurate with the lattice periodicity as one would expect for an antiferromagnet with a fixed spin on each lattice site. The adjective 'itinerant' is used because the spins that order belong to the mobile conduction electrons which give rise to the electrical conductivity [12]. This results in a spatially modulated electron spin polarization which is referred to as a spin density wave (SDW) state.

Lomer [13] pointed out that the electron Fermi surface at Γ (0,0,0), and the hole surface at H (1,0,0) in reciprocal space, almost have identical shapes as shown in figure 3.5.

If the electron surface at Γ is shifted by the wave vector $\pm Q$, where $Q = \frac{2\pi}{a}(0.95, 0, 0)$, it will nest against the hole surface at H. The Fermi surface is then unstable to the formation of bound electron-hole pairs as a result of coupling of the surfaces by the attractive coulomb interaction. At the critical temperature, T_N, a condensation of such electron-hole pairs thus occurs. The periodicity of the resulting SDW causes gaps in the energy spectrum for pairs of states separated by Q. If this nesting were perfect, each electron at the Fermi surface would see a hole state displaced by wave vector Q and both surfaces would be completely removed from the Fermi surface yielding insulating behavior. In fact, in chromium the nesting is not perfect; there are some differences in the shapes of the electron and the hole surfaces, such that part of the hole surface at H, as well as the hole ellipsoids at N remain, and thus chromium retains some of its metallic properties below T_N, though the electrical conductivity and electronic specific heat are reduced substantially [14].

Overhauser [15] noted the similarity between the spin density wave properties of chromium and the BCS theory of superconductivity. That is, a gap-like absorption is expected at an energy characteristic of the gap and a delta-function contribution to the optical conductivity is expected at $\omega = 0$ from the magnetic portion of the Fermi surface that vanishes.

Optical measurements were first carried out by Hughes and Lawson [16], in an attempt to observe the energy gap predicted by Overhauser [15] and Fedders and Martin [17]. Their measurements however showed no temperature-dependent structure. More careful measurements carried out by Rice *et al.* [18], reported the first observation of the optical energy gap which had a value of 0.137 eV. Another optical study by Bos and Lynch [14], reported an energy gap for pure chromium of 0.13 eV at 4 K. Barker and

Ditzenberger [19] measured the energy gap to be 0.137 eV.

The optical structure associated with the partial gap that forms is a sharp dip appearing in the reflectance spectrum. This gives rise to a peak in the real part of the optical conductivity whose location and shape are temperature dependent. As the temperature is raised from 80 K to 200 K the peak broadens and moves to lower energy [20].

3.5.2 Results

Two different samples of chromium were measured. Both were crystals with a well-defined face of hexagonal geometry selected from a 10 g batch of Alpha-Aesar 99.99% pure chromium crystallite pieces. In each case, the reflectance was measured using the procedure described previously for silicon with the exception that the chromium samples were examined at several temperatures: 323 K, 300 K, 172 K, and 79 K. To cool the sample liquid N_2 was poured into the cold finger. The heater was then used to stablize the desired temperature.

During data collection at temperatures below 200 K an unwanted absorption feature appears near 3000 cm^{-1}, which is due to absorption in a very thin layer of ice which develops over time. The deposition of ice, and hence the appearance of this feature was minimized by wrapping a heating tape around the cryostat before collecting data at low temperatures, and by warming the cryostat and the sample to 323 K each time before cooling to liquid Nitrogen temperatures.

Figure 3.6(a) shows the mid-infrared reflectance of chromium obtained for one of the samples using this system. Both samples gave virtually identical results.

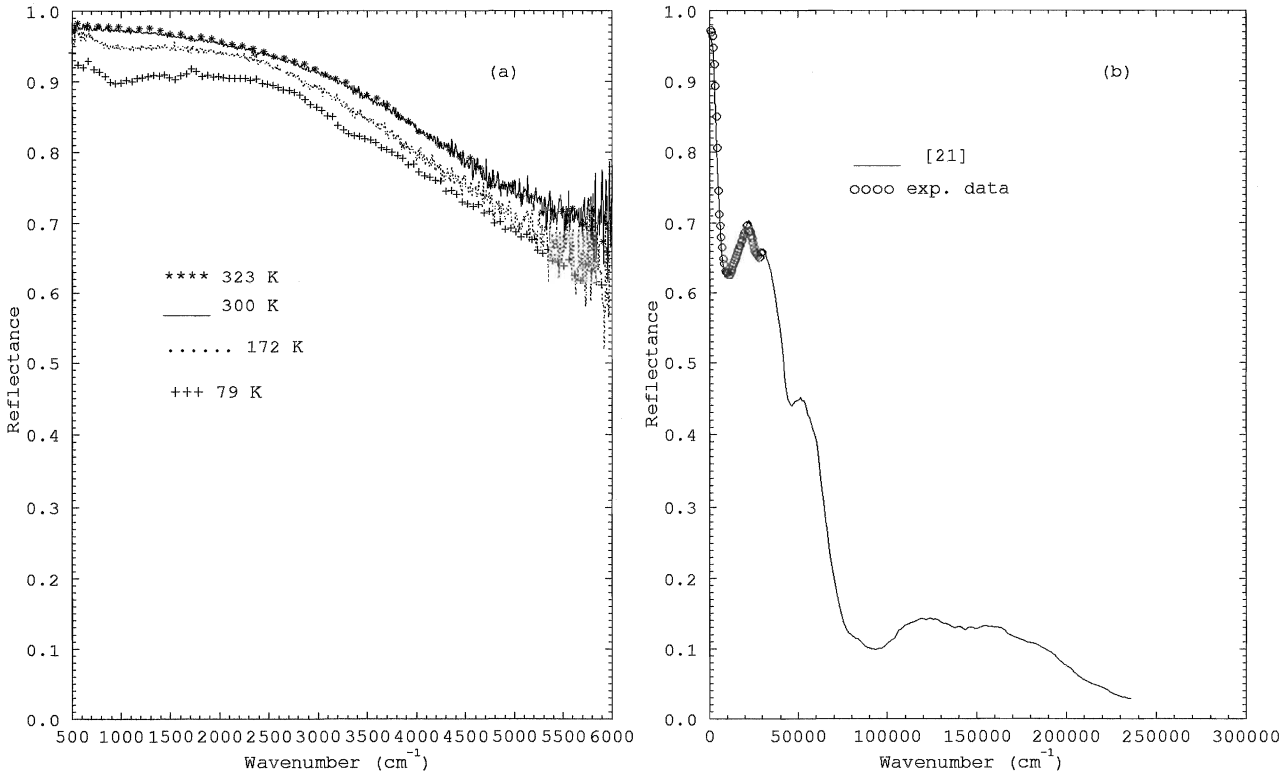

Figure 3.6: (a) The reflectance of Chromium at several temperatures in the mid-infrared. Note the dip which appears near 1000 cm^{-1} at low temperatures due to the formation of a SDW gap. The smaller dip near 3200 cm^{-1} in the 79 K spectrum is due to absorption in a thin layer of ice. (b) The reflectance of chromium at room temperature compared to literature data from Reference[21].

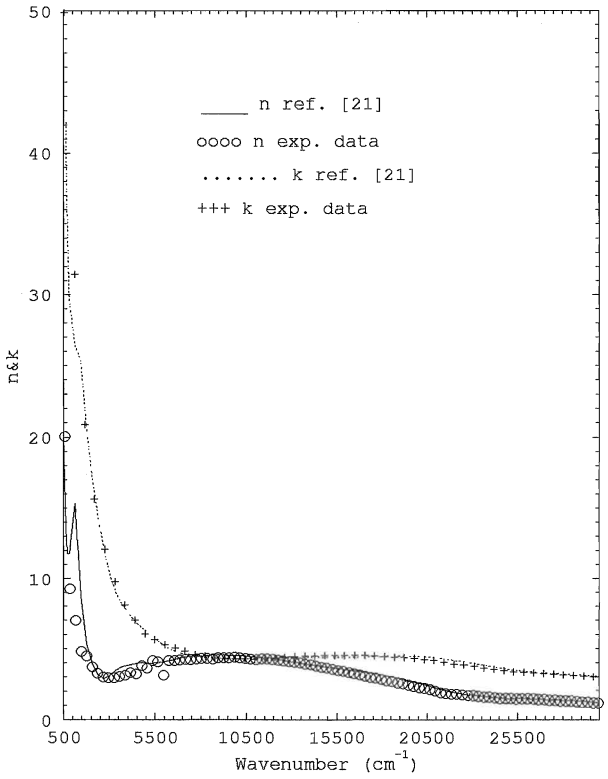

Figure 3.7: The real and imaginary parts of the refractive index of chromium at 300 K obtained in this work in comparison to those given in reference [21].

As expected, as the temperature is lowered below the Nèel temperature a dip appears in the reflectance near 1000 cm^{-1}. This absorption feature, due to the formation of the SDW gap, is seen as expected, very clearly at 79 K. At the lowest frequencies measured, the 300 K reflectance is slightly depressed from that at 323 K.

As a test of the reliability of the system to provide accurate results, a Kramers-Kronig analysis is desirable in order to make comparisons with optical constants given in the literature. The reflectance measurements were thus extended to 30000 cm^{-1} at room temperature using a grating spectrometer system described previously by Braun [22]. The combined room temperature results from both systems are shown in figure 3.6(b) along with a comparison to the reflectance calculated from n and k values given in reference [21]. There is very good agreement between the literature data and that obtained in this work. The minimum in the reflectance near 10000 cm^{-1} is due to an interband optical transition.

3.5.3 Data Analysis and Discussion

A Kramers-Kronig transformation, described in Chapter 4, was carried out to obtain the optical constants n and k and the optical conductivity. For this analysis, the experimental chromium reflectance from different spectral regions, interpolated to obtain evenly spaced data sets and linked together (500 - 30000 cm^{-1}) as shown in Fig. 3.6(b), was used. At low frequencies a linear extrapolation to R = 1 at zero frequency was made. Beyond the literature data at high frequencies an extrapolation of ω^{-4} was used in accordance with a Drude free-electron model [23]. Figure 3.7 shows the optical constants n and k obtained for chromium at room temperature from the present work along with data from References [20] and [21]. The optical conductivity obtained from the present work at 300 K is shown between 500 and 30000 cm^{-1} in Figure 3.8 compared

to results from References [20] and [21]. Note that the minimum in the reflectance at 10000 cm^{-1} due to an interband optical transition appears as a peak in the optical conductivity at 15000 cm^{-1}. Note as well the free carrier absorption at low frequencies. Table 3.1 provides values of the optical constants of chromium at selected frequencies at room temperature for further comparison of the results obtained in this work with those in the literature.

Figure 3.9 shows the temperature dependence of the optical conductivity obtained in the mid-infrared. The most distinctive temperature-dependent feature in the real part of σ is a peak near 1000 cm^{-1} which appears due to the formation of the SDW gap as the sample is cooled to 79 K. This peak is smaller in magnitude and shifted towards lower frequencies at 172 K and is not detectable at the higher temperatures measured. The temperature-dependence of this feature is in a good agreement with Reference [20]. The magnitude of the SDW gap can be determined from the frequency at which an onset of absorption is observed in the antiferromagnetic portion of the optical conductivity. However since there is a remaining Drude-like contribution to the optical conductivity in this region of the spectrum as well as some contribution from the tail of the higher frequency interband transitions this is difficult to extract unambiguously. The location of the peak which develops can be used as an estimate. This gives a value of 1200 cm^{-1} or 0.149 eV for the SDW gap.

3.6 Conclusion

The results of the 100% line and the leakage signal tests, show respectively that sample/reference repositioning, and the ability of the system to reject unwanted signal are reliable. The 100% line was found to be $1\pm$ 0.001 over the entire spectral range

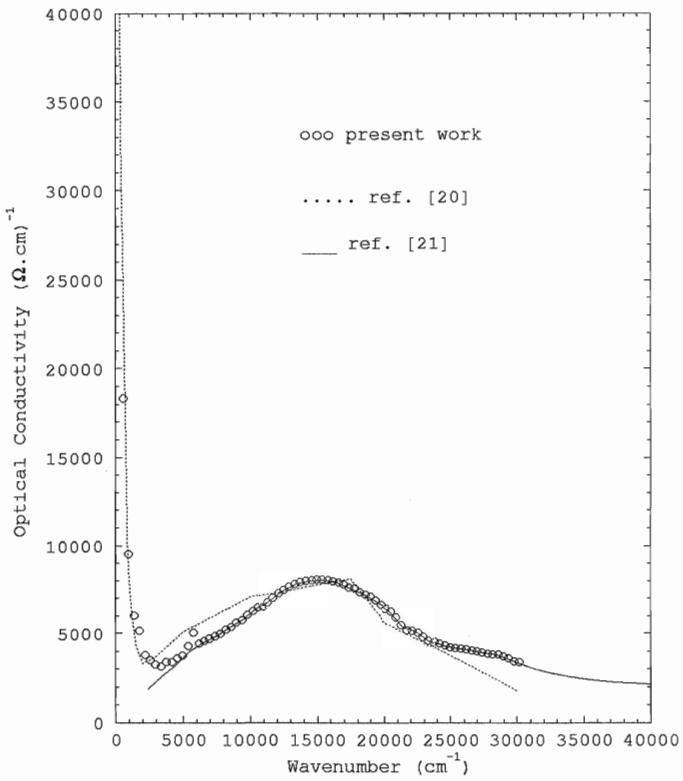

Figure 3.8: The optical conductivity of chromium at room temperature. Note the good agreement with the literature results.

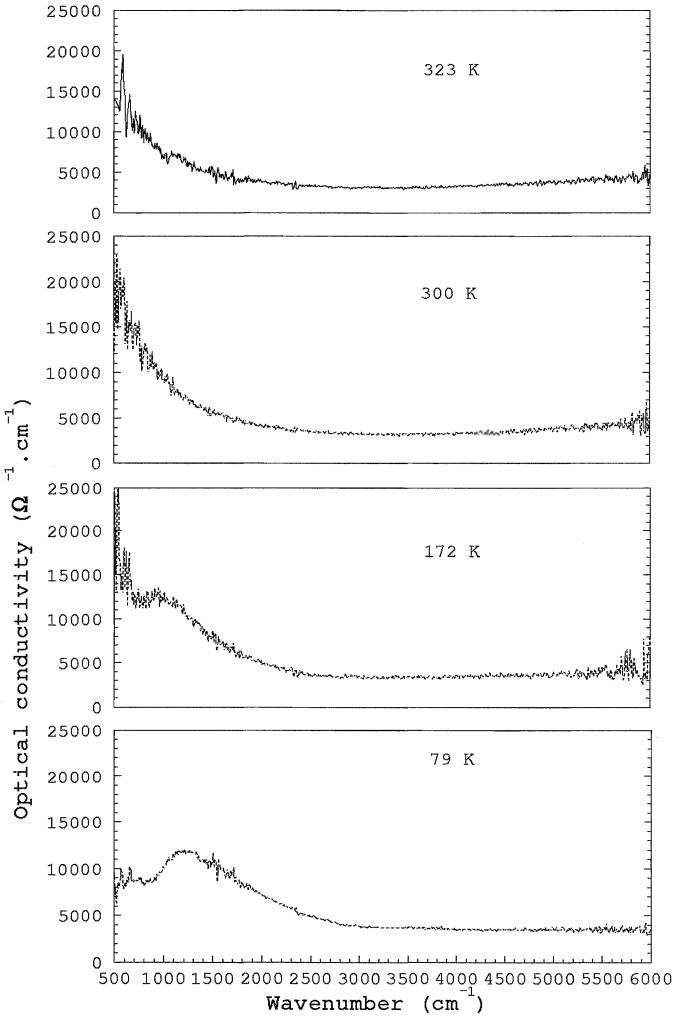

Figure 3.9: The mid-infrared optical conductivity of Chromium at different temperatures. Note the absorption peak which appears at low temperatures due to the formation of a SDW gap.

investigated, while the leakage signal observed was virtually negligible.

From the good agreement observed between the silicon and chromium reflectance data of this work and that of References [11], [20], and [21], as well as the agreement between the optical constants obtained by K-K analysis and literature data, one can conclude that the system is capable of producing accurate and reliable results, and can therefore be used to investigate samples with less well-known optical properties, which is the main goal of this thesis. The following chapter will focus on a study of the optical properties of the semiconductor Tin Telluride and several intentionally-doped alloys.

Table 3.1: The optical constants of Chromium at selected frequencies: σ' is the real part of the optical conductivity, δ is the skin depth $= \lambda/4\pi k$, and n and k are the real and imaginary parts of the index of refraction, N.

Reference	ω (cm^{-1})	$\sigma'(10^4)$ $(\Omega.cm)^{-1}$	n	k	$\delta(\dot{A})$
Present work (K-K)	5000	0.38	3.66	6.28	253.4
	15000	0.8	3.59	4.49	118
	20000	.65	2.27	4.27	93
	30000	0.33	1.14	2.94	90
Ref. 10 Reflectivity fits	5000	0.51	4.55	6.72	237
	15000	0.78	3.4	4.63	115
	20000	0.57	1.82	4.5	88
	30000	0.18	.64	2.83	94
Ref. 6 (K-K)	5000	0.39	4.11	6.3	252.6
	15000	0.8	3.48	4.3	123
	20000	0.62	2.5	4.4	91
	30000	0.32	1.15	3.01	88

Chapter 4

Theory

4.1 Introduction

When a beam of light is incident on an opaque sample surface, it will, depending on the angle of incidence and the refractive index, be partially or completely absorbed by the sample, with the remainder reflecting from the surface. Measuring the optical reflectance of light at normal incidence can provide a great deal of information regarding the electronic structure of the sample. Kramers-Kronig techniques are a widely used method to obtain the optical constants from the measured reflectance. Another method often used to analyze the measured reflectance is fitting to an oscillator model for the dielectric function.

In this chapter, Kramers-Kronig analysis and the Lorentz-Drude model will be briefly discussed in sections 4.2 and 4.3 respectively. Section 4.4 discusses the fitting procedure used in Chapter 6.

The following References were consulted in preparing the material presented in this chapter: [24, 25, 26, 27, 28, 29, 30, and 31].

4.2 Kramers-Kronig analysis

Kramers-Kronig analysis is a mathematical process, allowing one to calculate the phase (θ), and complex refractive index (N) of a sample from the measured reflectance.

$$N = n + ik, \tag{4.1}$$

where n and k are the real part and the imaginary part (known as the extinction coefficient) of N respectively. The reflectance at normal incidence is given in terms of n and k as:

$$R = \frac{(n-1)^2 + k^2}{(n+1)^2 + k^2}. \tag{4.2}$$

The measured reflectance at normal incidence, R, is given by:

$$R = \hat{r}(\omega)\hat{r}^*(\omega), \tag{4.3}$$

where

$$\hat{r} = \frac{n - 1 + ik}{n + 1 + ik}, \tag{4.4}$$

the complex reflectivity amplitude, $\hat{r}$, can be written as:

$$\hat{r} = r(\omega)e^{i\theta(\omega)}, \tag{4.5}$$

and

$$R = r^2(\omega), \tag{4.6}$$

where θ is the phase difference between the electric field of the incident and reflected waves. Using Equations 4.4 and 4.5, n is given by:

$$n = \frac{1 - r^2}{1 + r^2 - 2r\cos\theta}, \tag{4.7}$$

and k by:

$$k = \frac{-2r\sin\theta}{1 + r^2 - 2r\cos\theta}. \tag{4.8}$$

The phase difference between the incident and the reflected wave is obtained via a Kramers-Kronig relation as [25]:

$$\theta(\omega') = \frac{1}{\pi}\int_0^\infty \frac{d\ln r}{d\omega} ln\left|\frac{\omega + \omega'}{\omega - \omega'}\right| d\omega. \tag{4.9}$$

Because the reflectance is measured over a finite range, the integration must be done numerically, and extrapolation of the results in regions where data is not available is necessary. For example the lowest frequency data must be extrapolated to R = 1 at zero frequency or an oscillator fit to the reflectance data can be used. For high frequencies, the reflectance can be described by the free-electron limit. That is, it goes as ω^{-4}. The complex dielectric function $\epsilon(\omega)$, is given by [27]:

$$\epsilon(\omega) = \epsilon'(\omega) + i\epsilon''(\omega), \tag{4.10}$$

where the real part is:

$$\epsilon' = n^2 - k^2, \tag{4.11}$$

and the imaginary part is:

$$\epsilon'' = 2nk. \tag{4.12}$$

The complex optical conductivity can be calculated from the dielectric function as follows:

$$\sigma(\omega) = \sigma'(\omega) + i\sigma''(\omega), \tag{4.13}$$

where the real part of σ is:

$$\sigma'(\omega) = \frac{\omega\epsilon''(\omega)}{4\pi}, \tag{4.14}$$

and the imaginary part of σ is:

$$\sigma''(\omega) = \frac{\omega(1 - \epsilon'(\omega))}{4\pi}. \tag{4.15}$$

4.3 Drude-Lorentz Model

Solids may be divided into three main classes: insulators, metals, and semiconductors. This classification is based on their energy band structure. The Lorentz model can be used to describe direct interband transitions, which occur when a photon excites an electron to another band. This model is applicable to insulators. The Drude model is used to describe metals. It models the absorption arising from the excitation of carriers in a partially filled band from filled states below the Fermi energy to empty states within the same band above the Fermi energy. Most real materials, including semiconductors,

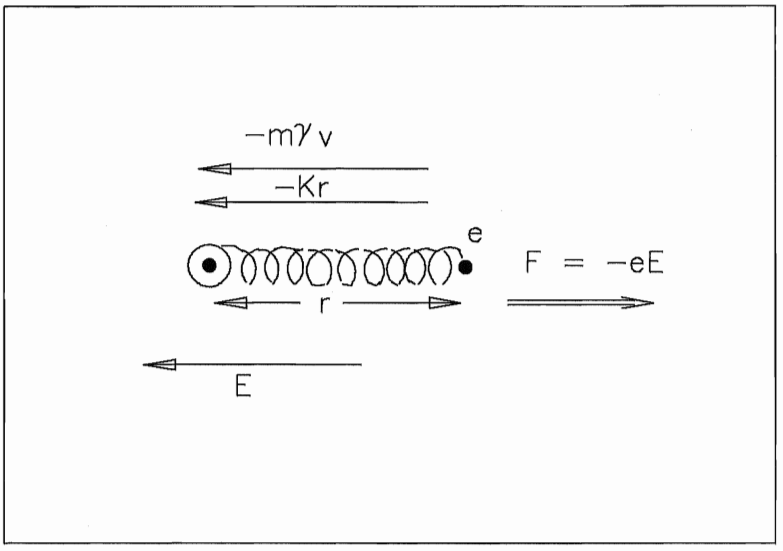

Figure 4.1: The atomic dipole in the presence of an electric field.

can be described with a combination of these two models.

The motion of an electron with mass m and charge e, shown in figure 4.1, can be written as:

$$-Kr - m\gamma\frac{dr}{dt} + eE = m\frac{d^2r}{dt^2}, \tag{4.16}$$

where Kr is a Hooke's law restoring force which binds the electron to the nucleus, and K is the restoring force constant given by: $K = m\omega_0^2$, where ω_0 is the resonance frequency. The second term represents the damping force and arises from the various scattering mechanisms that exist in solids. γ is the damping constant, which is related to the relaxation time, τ, by $\tau = \frac{1}{\gamma}$. The eE term is the driving force, where E is the electric field.

The polarization P, which is the dipole moment per unit volume, is given by:

$$P = per, \tag{4.17}$$

where p is the number of electrons per unit volume, and r is the distance between the positive and negative charge. The electric field is described by:

$$E = E_0 e^{-i\omega t}. \tag{4.18}$$

For a solution of the form:

$$r = r_0 e^{-i\omega t}, \tag{4.19}$$

the first time derivative of r is:

$$\frac{dr}{dt} = -i\omega r, \tag{4.20}$$

and the second time derivative of r is:

$$\frac{d^2r}{dt^2} = -\omega^2 r. \tag{4.21}$$

If one substitutes by 4.19, 4.20, and 4.21 into equation 4.16, one finds:

$$r = \frac{eE}{-m\omega^2 - im\omega\gamma + K}. \tag{4.22}$$

The polarization given in equation 4.17 can thus be written as:

$$P = \left[\frac{pe^2}{-m\omega^2 - im\omega\gamma + K}\right] E. \tag{4.23}$$

The complex dielectric function is given as:

$$\epsilon = 1 + \frac{4\pi P}{E}. \tag{4.24}$$

Substituting equation 4.23 into equation 4.24 gives:

$$\epsilon = \epsilon' + i\epsilon'' = 1 + \frac{4\pi p e^2}{-m\omega^2 - im\omega\gamma + K}, \tag{4.25}$$

which can be written as:

$$\epsilon = 1 + \frac{\omega_p^2}{\omega_0^2 - \omega^2 - i\gamma\omega}, \tag{4.26}$$

where ω_p is the plasma frequency, given as:

$$\omega_p^2 = \frac{4\pi p e^2}{m}. \tag{4.27}$$

In a real solid there are several such absorption processes and the dielectric function can be written as :

$$\epsilon = \epsilon_{FC} + \epsilon_{BC} + \epsilon_{LV}, \tag{4.28}$$

where the first term is a free carrier contribution, the second term is the bound carrier contribution, and the third term is the contribution of lattice vibrations to the dielectric function. In the free electron model (Drude-Model) there is no restoring force, and thus ω_0 is zero. The total dielectric function for a material exhibiting both free carrier and bound carrier absorption is thus given as:

$$\epsilon = 1 + \frac{\omega_p^2}{-\omega^2 - i\gamma\omega} + \epsilon_{BC}. \tag{4.29}$$

Here the second term is the free carrier contribution. Lattice vibrations can be modeled by terms of the form of the bound carrier contribution. However, in the infrared spectral region, the lattice vibrations typically make only a small contribution to the dielectric function. The bound carrier contribution at frequencies lower than the fundamental absorption edge becomes frequency independent, and is renamed the optical dielectric constant (ϵ_∞). In such cases, the dielectric function can be written as:

$$\epsilon = \epsilon_{FC} + \epsilon_\infty. \tag{4.30}$$

Where ϵ_{FC} is given as:

$$\epsilon_{FC} = -\frac{4\pi p e^2}{m_s} \frac{1}{\omega^2 + \gamma^2} \left(1 - i\frac{\gamma}{\omega}\right). \tag{4.31}$$

Here p is the free carrier concentration, and m_s is the electron effective mass, which may be different from the scalar electron mass m. That is, in real materials the electron may respond to external forces as if it was a free electron of mass m_s.

4.4 Fitting To A Model Dielectric Function

In general the reflectance or any of the Kramers-Kronig derived optical functions can be fit to the model discussed in section 4.3. Each bound absorption process has three variable parameters associated with it (ω_{p_i}, ω_{0_i}, and γ_i where i signifies the i^{th} bound absorption process) while the free-electron Drude term has two ($\omega_{p_{FC}}$ and γ_{FC}). ϵ_∞ is also a parameter of the fit.

Chapter 5

Reflectance Measurements of Mn and Pb-doped SnTe

5.1 Introduction

Tin Telluride is a semiconductor with the NaCl crystal structure. It is always p-type as a result of a high concentration of Sn vacancies, which is in the range of 10^{19} to 10^{21} cm^{-3} [32].

Studies of the thermal and electrical properties of SnTe indicate that this semiconductor has a complex band structure [33].

Studies have been carried out of the optical properties of SnTe on samples having carrier concentrations ranging from 3.6×10^{19} to 1×10^{21} cm^{-3}. It was found that the optical properties in the mid and near infrared regions arise from both bound and free carrier absorption, each dominating, respectively, in the high and low energy regions.

The mid infrared reflectance is characterized by a pronounced plasma edge found to be well explained by means of a Drude free carrier model [23, 32, 34, 35, 36, 37, 38, 39, 40]. Carrier concentration dependent changes in the absorption coefficient, α, the effective mass of the carriers, m_s, and the contribution from bound carriers, have a pronounced effect on the reflectivity curve [34, 36, 37]. The effective mass of the free carriers was found to be surprisingly small (the effective mass ratio, m_s/m_e, for SnTe

with carrier concentration ranging from 1 to 5 $\times 10^{20}$ cm^{-3} is found to be in the range 0.08 to 0.14) and to decrease with decreasing hole concentration [34]. A relationship between the wavelength of the reflection minimum and the carrier concentration was noticed by Gobachev *et al.*, who found that the minimum in the reflectance is shifted towards shorter wavelengths with increasing carrier concentration [35]. The effect of decreasing temperature is manifested in a sharpening and a shift of the location of the minimum to higher frequencies [40].

The indices of refraction corresponding to bound carrier absorption are large, and carrier concentration dependent. At energies lower than the fundamental absorption edge (the energy corresponding to the rapid rise in absorption due to bound carriers [41]), the bound carrier absorption becomes wavelength independent and their contribution to the dielectric function can be represented by the optical dielectric constant ϵ_∞. Significant shifts were revealed in the location of the fundamental absorption edge with carrier concentration, and are believed to be the result of changes in the Fermi energy [34].

SnTe can be doped for example with Ag, Pb, and Mn to produce wide variation in carrier concentration [42], [43], and [44]. In Mn-doped alloys, the Mn ion exists as Mn^{++} with a spin of 5/2. The magnetic ions are randomly distributed in the metallic fcc sublattice of the rock salt crystal lattice. The resistivity of these alloys has a metallic temperature-dependence and its magnitude increases with increasing Mn concentration [45, 46, 47, and 48]. At very low temperatures, alloys with a low concentration of magnetic Mn^{++} ions are spin glasses, while those with higher concentrations exhibit ferromagnetic or antiferromagnetic phases [42, 43].

There have been few optical studies of intentionally Mn and Pb-doped SnTe. The

first study of the Mn-doped system was carried out by Escorne and Mauger [44], who measured the reflectance of $Sn_{0.923}Mn_{0.077}Te$ and SnTe samples with similar carrier concentration (6.2×10^{20} cm^{-3} and 6.6×10^{20} cm^{-3} respectively) in the infrared region (1666-10000 cm^{-1}), at various temperatures. The optical parameters m_s, ϵ_∞, and the optical mobility μ were determined by Drude fitting to the measured reflectance. Their results showed that these parameters are temperature-dependent, where m_s decreases with decreasing temperature, while ϵ_∞ and μ decrease with increasing temperature, and are in agreement with those of references [37] and [40] for SnTe. Their results also showed that there is no significant difference in m_s for the SnTe and the Mn-doped SnTe samples down to 13 K, which implies that adding 7% Mn has no significant effect on the band structure of SnTe.

Korn and Braunstien [23, 39], studied the optical properties of $Pb_{1-x}Sn_xTe$ with carrier concentration ranging from 8×10^{18} cm^{-3} to 7.5×10^{20} cm^{-3}. This alloy has very interesting properties in the spectral range from 2 to 16 micron (600-5000 cm^{-1}). As x decreases from 1 to 0, the energy gap approaches zero. This property makes this alloy system an interesting material for infrared device applications, such as infrared detectors [39]. The infrared reflectivity of the samples was measured at 80 and 300 K and the optical parameters were obtained from Drude fitting to the measured reflectance. The effective mass was found to remain non-zero as the energy gap approached zero. This result is consistent with the anomalous behavior of the temperature-dependence of the effective mass of SnTe reported by Bis and Dixon [37], who found a decrease in m_s upon increasing the band gap by lowering the sample temperature.

The focus of this chapter is a study of the optical properties of the semiconductor Tin Telluride, and several substitutional Lead, and Manganese alloys. The samples that

were measured are, pure Tin Telluride (SnTe), $(SnTe)_{98}(MnTe)_2$, $(SnTe)_{95}(MnTe)_5$, and $[(PbTe)_{75}(SnTe)_{25}]_{95}(MnTe)_5$. The reflectance measurements cover the range from 500 to 30000 cm^{-1} at room temperature, and from 500 to 6000 at temperatures down to 79 K. The optical conductivity and other related parameters are presented.

5.2 Sample Preparation

For each compound a small piece of polycrystalline material was selected for the reflectance measurements and hand polished as described in Chapter 3. Mirror like surfaces were prepared. A rectangular piece from each sample with dimensions given in Table 5.1, was prepared for resistivity measurements.

5.3 Mid-Infrared Reflectance Measurements

The same methods and techniques used for measuring the reflectance of chromium, described earlier in Chapter 3, were used to measure the mid-infrared reflectance of these samples.

5.4 Near-Infrared-Visible-UV Reflectance Measurements

For frequencies higher than 6000 cm^{-1}, the reflectance at room temperature was measured using a grating spectrometer system. Reflectance measurements were carried out in two stages. The reflectance in the region from 250 to 800 nm (12500-40000 cm^{-1}), was measured using a UV360 Silicon photodiode detector, and a Xenon arc lamp light source. A Corion BG3 filter was used in the range from 250 to 500 nm (20000-40000 cm^{-1}), while a green glass filter covered the range from 420 to 820 nm (12195-23800 cm^{-1}). The absolute reflectance was determined by overcoating the sample with Aluminum and making the appropriate correction [11]. The reflectance in the region

from 800 to 1900 nm (5200-12500 cm^{-1}) was measured using a PbS detector and a tungsten lamp light source. A U330 filter was used in the range from 800 to 1200 nm (5200-12500 cm^{-1}) and an Oriel filter was used for the range from 1100 to 1900 nm (5200-9000 cm^{-1}). In this spectral region, a gold overcoating was used to determine the absolute reflectance. Further details regarding this system can be found elsewhere [22].

5.5 Resistivity Measurements

Room temperature resistivity measurements were carried out using a four point probe technique. Gold wires, of 0.025 mm diameter were attached to the sample with silver paint in the geometry shown in Figure 5.1. The resistivity was calculated from the measured resistance, R, as follows:

$$\rho = \frac{R \times A}{L}, \tag{5.1}$$

where A and L are the cross-sectional area and the distance between voltage contacts respectively. The estimated carrier concentration (p), the measured resistivity at room temperature (ρ), and the dc-conductivity (σ) of the samples, determined from $\sigma = \frac{1}{\rho}$, are given in Table 5.1.

Table 5.1: Cross-sectional area, A in mm^2, distance between voltage contacts, L in mm, carrier concentration p, measured resistivity (ρ) and dc-conductivity (σ) at 300 K, for SnTe and several Pb and Mn-doped alloys.

sample	A	L	p $\times 10^{20}$ cm^{-3}	$\rho \times 10^{-4}(\Omega.cm)$	$\sigma(\Omega.cm)^{-1}$
SnTe	3.8	1.8	4.0	2.05	4880
$(SnTe)_{98}(MnTe)_2$	3.0	1.1	6.0	1.80	5330
$(SnTe)_{95}(MnTe)_5$	2.5	1.0	3.8	4.00	2500
$[(PbTe)_{75}(SnTe)_{25}]_{95}(MnTe)_5$	2.1	1.6	1.7	35.50	280

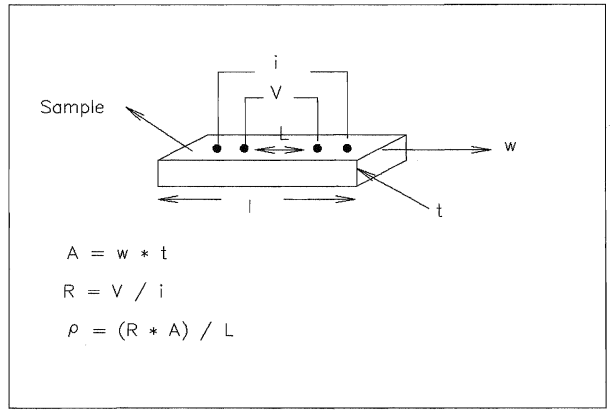

Figure 5.1: Configuration used for resistivity measurements.

5.6 Results

The reflectance of the samples at frequencies from 500 to 6000 cm^{-1} was measured at temperatures between 300 K and 79 K, as shown in Figure 5.2. The reflectance measurements at 300 K were extended to 30000 cm^{-1}. The room temperature reflectance over the entire range of frequencies investigated is shown in Figure 5.3.

Previous work on SnTe [37, 40], and Mn-doped SnTe [38] showed that with decreasing temperature, the plasma edge sharpens and the corresponding minimum in the reflectance becomes more pronounced and shifts to slightly higher frequencies. This is due to the temperature dependence of the optical parameters m_s, ϵ_∞, and γ, where the damping coefficient, γ, is primarily responsible for the width of the dip near the plasma frequency, and ϵ_∞ for the absolute value of the reflectance minimum, while the location of the minimum can be determined from the product $m_s\epsilon_\infty$ [38]. Figures 5.2 and 5.3 confirm this behavior for pure SnTe and the Pb and Mn-doped SnTe samples.

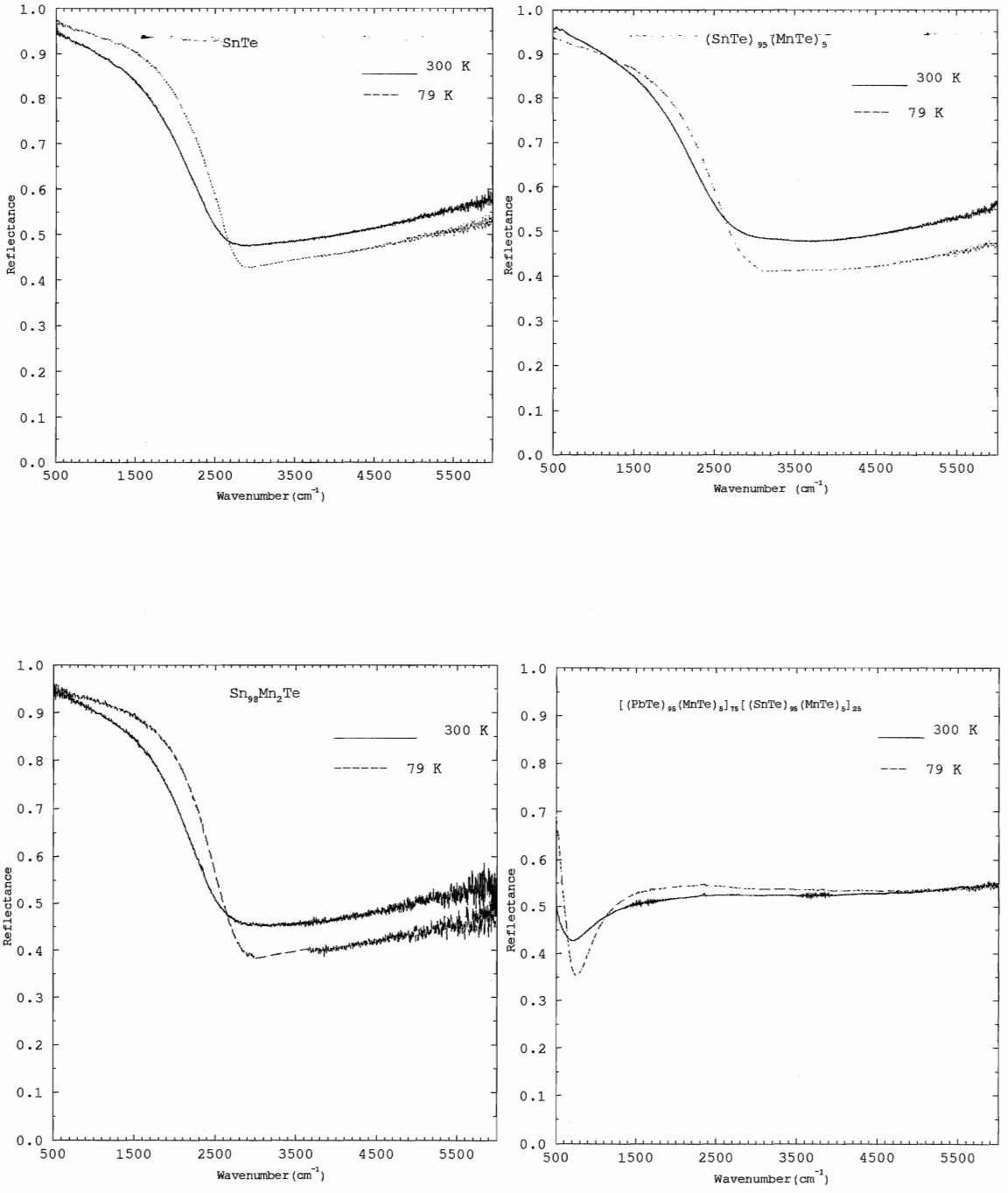

Figure 5.2: Measured reflectance of SnTe and the Pb/Mn-doped alloys at 300 and 79 K.

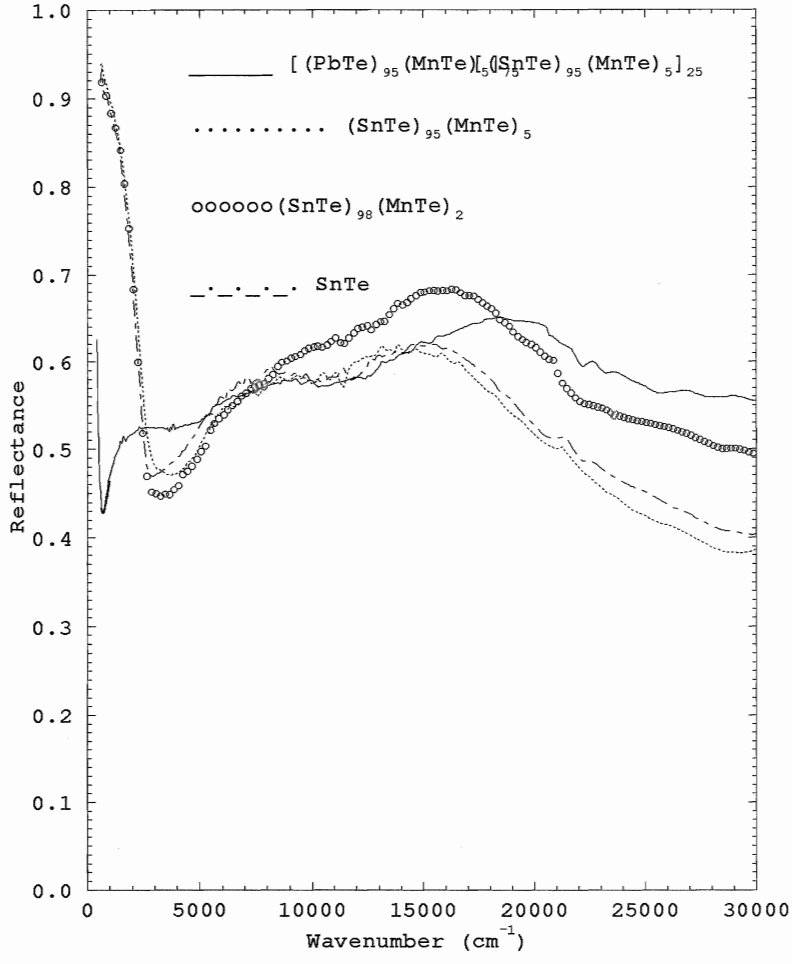

Figure 5.3: The reflectance of SnTe and the Pb/Mn-doped alloys at room temperature.

As shown in Figure 5.3, the strong dependence of the mid infrared reflectance on the free carrier concentration can be seen in the variation of the location, width, and depth of the reflectance minimum for the various SnTe and Mn/SnTe samples investigated. The free carrier concentration (p) for the SnTe, $Sn_{98}Mn_2Te$, and $Sn_{95}Mn_5Te$ samples investigated was estimated by comparing the observed location of the reflectance minimum to that of the curves for SnTe reported in References [34], [35], [37], and [38]. The results are shown in Table 5.1 and the uncertainty in these values is estimated to be 5%. The free carrier concentration for $[(PbTe)_{75}(SnTe)_{25}]_{95}(MnTe)_5$ was estimated by comparing the measured reflectance to the reflectance of Pb/SnTe samples, reported in Reference [23]. Because the plasma edge did not match exactly any of the ones reported in Reference [23], the uncertainty in this latter estimate is higher.

5.7 Data Analysis and Discussion

The complex refractive index, N, dielectric function, ϵ, and optical conductivity, σ, of the samples were obtained by applying Kramers-Kronig analysis to the measured reflectance, as explained earlier in Chapter 3. The real part of the optical conductivity at room temperature is shown in Figure 5.4. The peak in the optical conductivity near 13000 cm^{-1} is associated with the broad peak observed in the reflectivity spectrum between 5000 and 30000 cm^{-1}, and is assigned to an interband transition from occupied valence band states across the Fermi level to empty conduction band states [23, and 49]. Figure 5.5 shows the real part of the optical conductivity at various temperatures. Note that the conductivity curve becomes flatter at frequencies higher than 3000 cm^{-1} as the temperature decreases. This feature becomes more significant in the Mn/SnTe alloys. The dc-conductivity and the low frequency limit of the optical conductivity at room temperature are found to be in good agreement for $Sn_{95}Mn_5Te$ and

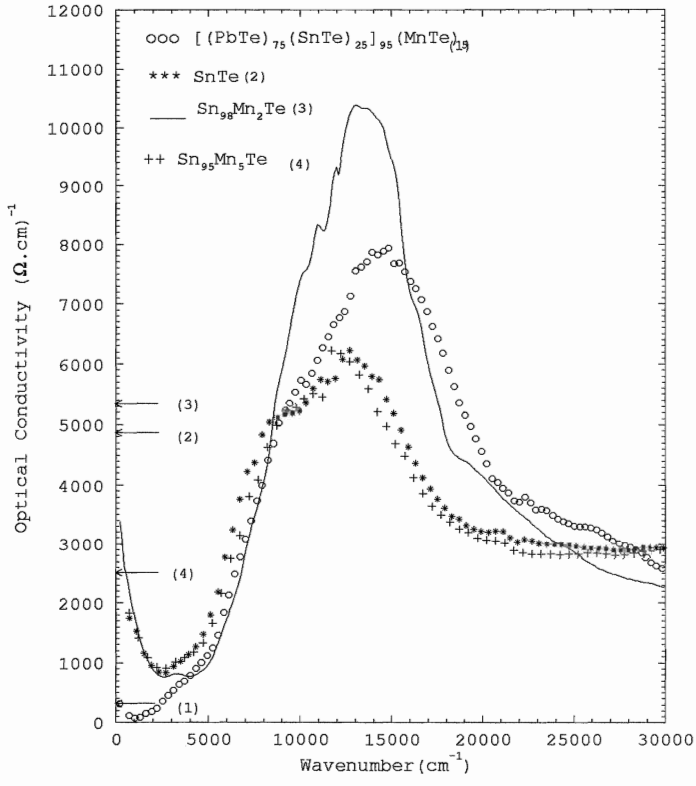

Figure 5.4: The optical conductivity of SnTe and several intentionally doped alloys at 300 K. The arrows show the dc-conductivity numbered according to the labels in the legend.

$[(PbTe)_{75}(SnTe)_{25}]_{95}(MnTe)_5$ as shown in Figure 5.4 where the dc-conductivity values are taken from Table 5.1. The optical conductivity at 500 cm^{-1} for the above mentioned samples is approximately 2450 $(\Omega.cm)^{-1}$ and 200 $(\Omega.cm)^{-1}$, while the measured dc-conductivity is 2500 $(\Omega.cm)^{-1}$ and 280 $(\Omega.cm)^{-1}$, respectively. The optical conductivity values for SnTe and $Sn_{98}Mn_2Te$ are lower than the dc-conductivity values by a factor of 2, however, these two samples have the highest carrier densities, and the Drude peak is not fully developed at 500 cm^{-1}.

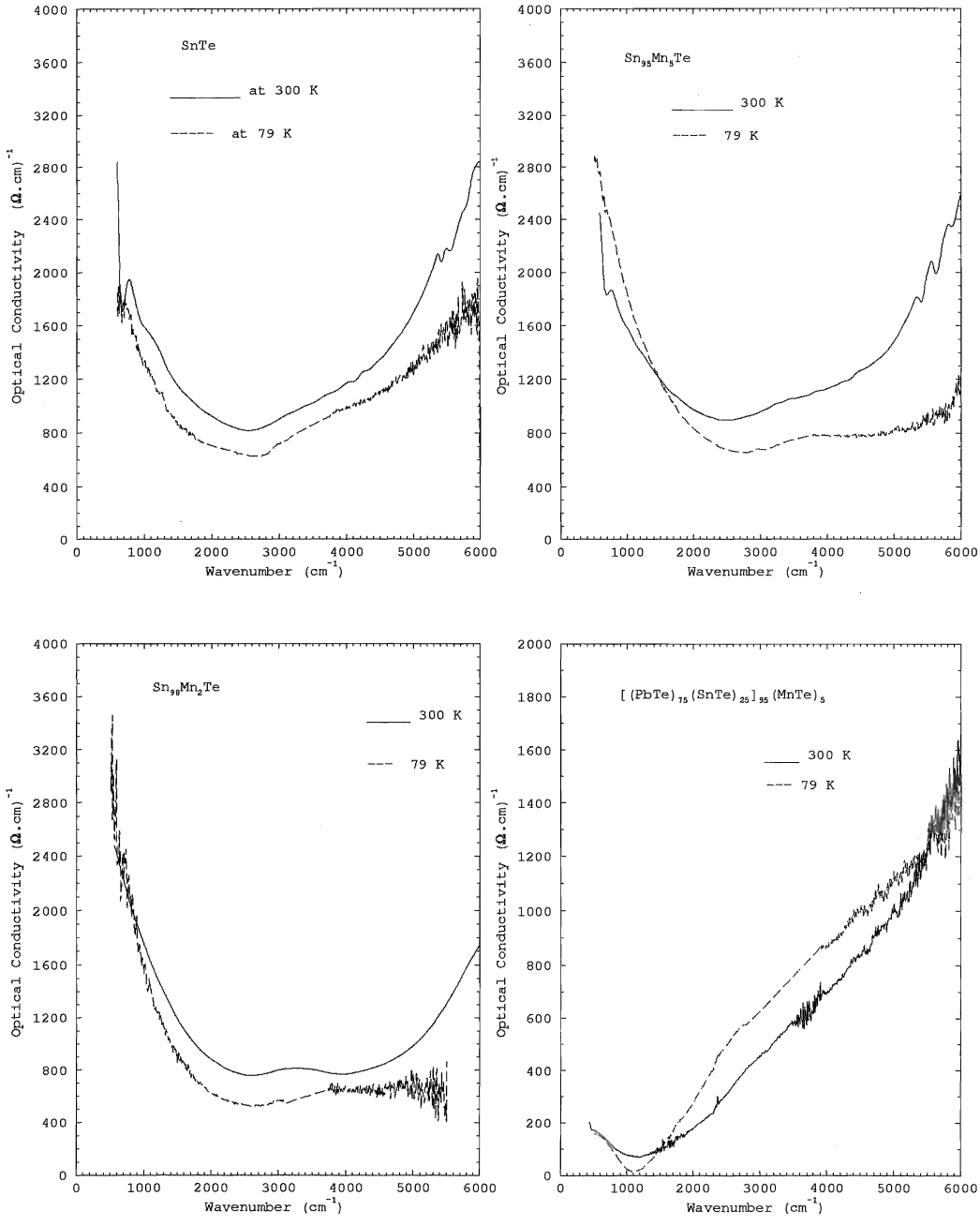

Figure 5.5: The mid-infrared optical conductivity of SnTe and Pb/Mn-doped SnTe alloys at 79 and 300 K.

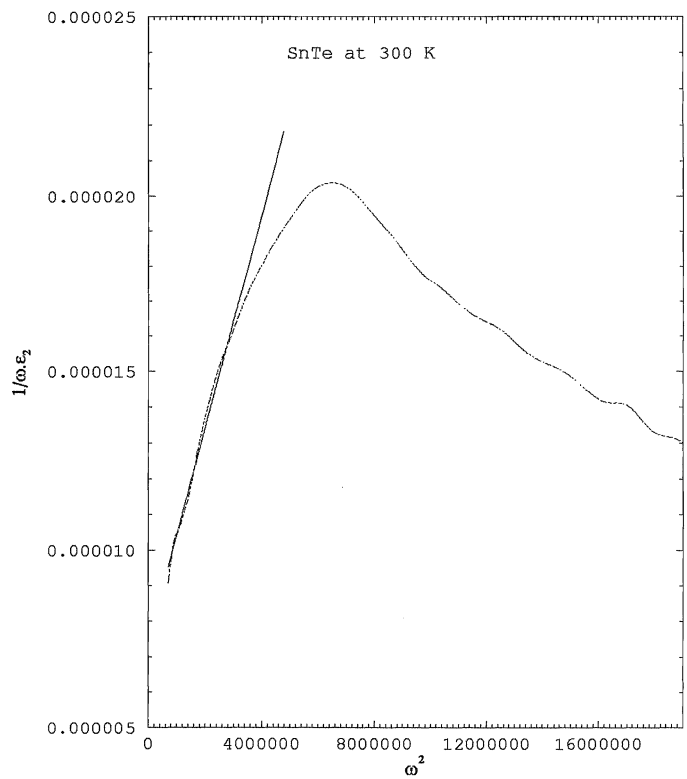

Figure 5.6: The reciprocal of $\omega\epsilon_2$ as a function of ω^2 for SnTe at 300 K. The slope and the intercept of the linear fit shown are used to extract γ and ω_p as explained in the text.

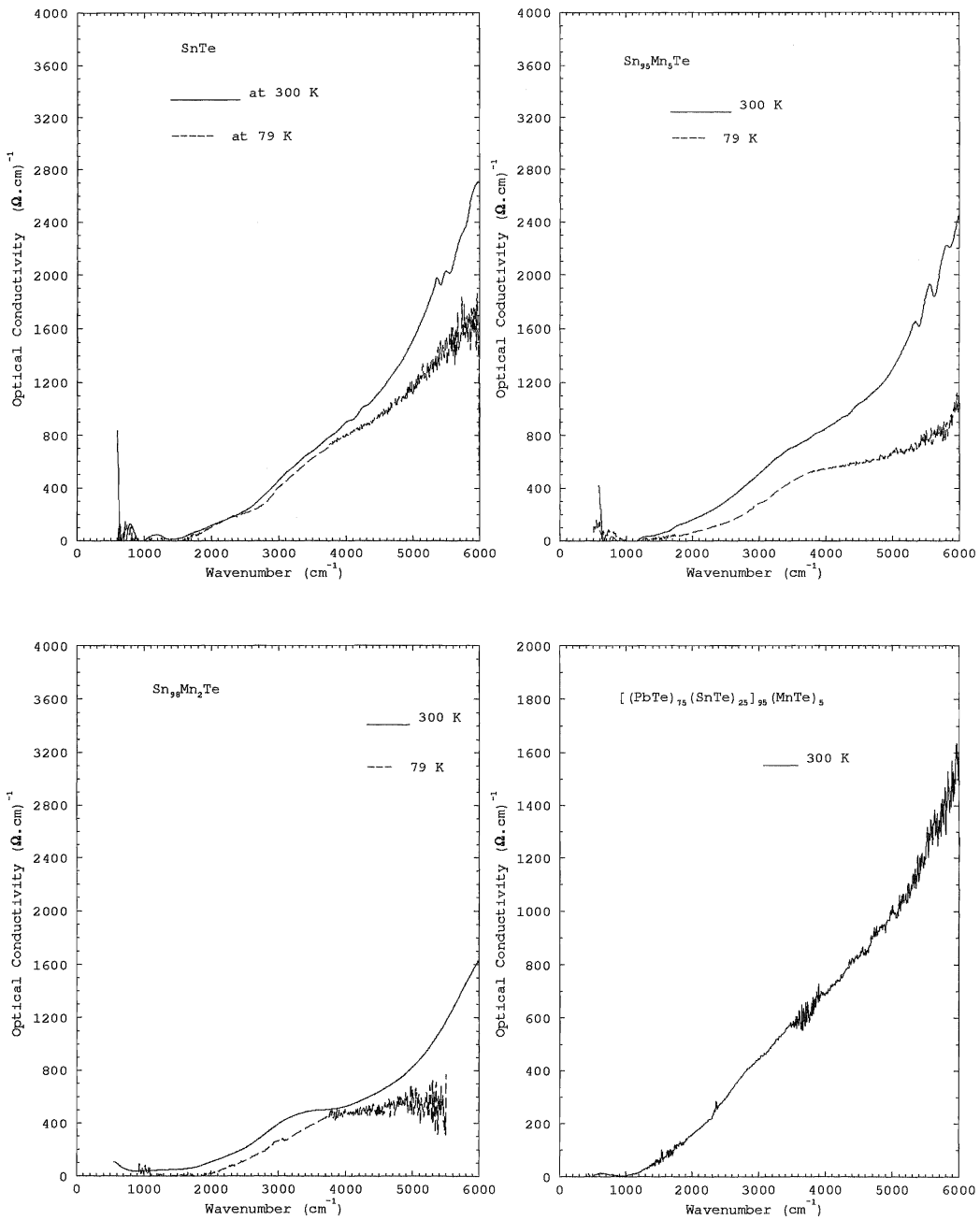

Figure 5.7: The absorption edge calculated as explained in the text.

In the spectral range governed by free carriers, $\frac{1}{\omega\epsilon_2}$ plotted as a function of ω^2 is expected, from Equation 4.31, to give a straight line. Figure 5.6 shows an example for SnTe at room temperature. Note the linear behaviour at the lowest frequencies as expected. The curve begins to deviate from this linear behaviour as a result of the onset of bound carrier absorption. A linear fit can be made. The ratio of the intercept (b) to the slope (m) gives γ^2, while ω_p^4 is determined from $\frac{1}{m \times b}$. The plasma frequency and the damping coefficient obtained via this method are presented in Table 5.2. The effective mass of the samples at room temperature is then calculated from ω_p, and the estimated free carrier concentration, using Equation 4.27, and also presented in Table 5.2.

Previous studies found the effective mass to increase with increasing carrier concentration, and to decrease with decreasing temperature [32, 34, 35, 36, 37, 38, and 46]. For samples having carrier concentration between 4×10^{20} and 6×10^{20} cm^{-3}, the ratio of the effective mass to the electron mass was found in these studies to be in the range of 0.14 to 0.17. The effective mass values at room temperature, presented in Table 5.2, show the expected carrier concentration dependence. The value obtained for SnTe is in agreement with the value given for a similar sample in Reference [37].

The plasma frequency, ω_p, was generally found to decrease with decreasing temperature. At 79 K, for Mn-doped samples, the ω_p values increase slightly and then drop again at 5 K for the $Sn_{98}Mn_2Te$ sample. This behaviour is similar to that observed for $Sm_2Mo_2O_{7-\delta}$, which like Mn-doped SnTe is also a metallic spin glass system at low temperatures [50]. The spin glass properties of $Sn_{98}Mn_2Te$ will be discussed in the following chapter. The scattering rate, γ, was found to decrease with decreasing temperature.

Figure 5.7 shows the absorption edge, which is calculated by subtracting the Drude

fit from the real conductivity curves. The Drude conductivity was calculated using the parameters ω_p and γ, given in Table 5.2, using Equations 4.14 and 4.31.

The above analysis could not be applied to the $[(PbTe)_{75}(SnTe)_{25}]_{95}(MnTe)_5$ sample at low temperatures, because there is not enough data in the low-frequency spectral range.

The resistivity of SnTe is found to increase with increasing temperature and to decrease with increasing carrier concentration [45, 47, 48, and 51]. For Mn-doped samples, the resistivity is dependent on the manganese concentration as well. As shown in Reference [45], it is found to increase with increasing concentration. Table 5.1 gives the measured dc-resistivity for the samples investigated in this study. As expected the resistivity of the sample with 5% Mn is higher than that with 2% Mn at room temperature. Table 5.2 lists values for the temperature dependence of the resistivity derived from the optical analysis. Although the uncertainty in these values is high the general trend is for the resistivity to remain constant or decrease with decreasing temperature; in reasonable agreement with the expected metallic behaviour.

5.8 Conclusion

An extended study of the reflectance of Pb and Mn-doped SnTe alloys has been carried out over a wider spectral range than any previous work. The optical conductivity of these alloys is presented for the first time.

The results of this study show that the reflectance and various deduced optical parameters are carrier concentration and temperature dependent, which agrees with the literature. No significant difference was found between the room temperature reflectance of the SnTe and the $Sn_{95}Mn_5Te$ samples investigated. These samples have almost the same carrier concentration, and virtually identical room temperature optical conductivity curves. Therefore one can conclude that the addition of a small amount of manganese for Sn has little effect on the room temperature band structure of SnTe, as reported in Reference [44]. At 79 K, the optical conductivity of Mn-doped SnTe decreases more than the optical conductivity of SnTe at higher frequencies.

The fundamental absorption edge was obtained by subtracting the calculated Drude conductivity from the total optical conductivity. It is clear that in the frequency range near the fundamental absorption edge, the optical properties of SnTe and the Pb/Mn-doped alloys arise from the contributions of both the free carriers and the bound carriers. Thus, one can conclude that the optical parameters, ω_p and γ, derived in this work are more accurate than those presented in the literature [35, and 46], and obtained from fitting the reflectance to the Drude form, which describes only the free carrier contribution.

The measured room temperature dc-conductivity values were found to be in agreement with values extrapolated to zero frequency from the optical conductivity curves for the $Sn_{95}Mn_5Te$ and the $[(PbTe)_{75}(SnTe)_{25}]_{95}(MnTe)_5$ samples. For $Sn_{98}Mn_2Te$ and SnTe a discrepancy of approximately a factor of two was found with the optical conductivity at the lowest measured frequency. Values for the resistivity derived from the optical analysis indicate a constant or metallic-like decrease with decreasing temperature.

Table 5.2: The optical parameters obtained from the imaginary part of the dielectric function, ϵ, as explained in the text.

sample	Temperature (K)	ω_p (10^4 cm^{-1})	γ (10^{14}s^{-1})	ρ (10^{-4} Ω.cm)	m_s/m_e
SnTe	323	1.52±0.15	0.436±0.2	3.7	
$p \approx 4 \times 10^{20}$ cm^{-3}	300	1.44±0.03	0.433±0.2	4.1	0.17
	172	1.40±0.09	0.379±0.2	3.8	
	79	1.31±0.15	0.358±0.2	4.1	
$Sn_{98}Mn_2Te$	323	1.48±0.05	0.368±0.12	3.3	
$p \approx 6 \times 10^{20}$cm^{-3}	300	1.46±0.13	0.364±0.11	3.3	0.24
	172	1.32±0.15	0.328±0.13	3.7	
	79	1.36±0.15	0.280±0.12	3.1	
	5	1.24±0.15	0.242±0.12	3.1	
$Sn_{95}Mn_5Te$	323	1.52±0.02	0.515±0.10	4.4	
$p \approx 3.8 \times 10^{20}$ cm^{-3}	300	1.43±0.10	0.438±0.12	4.2	0.16
	172	1.42±0.15	0.414±0.10	4.0	
	79	1.48±0.06	0.32±0.10	2.9	
$[(PbTe)_{75}(SnTe)_{25}]_{95}(MnTe)_5$	323	0.34±0.01	0.166±0.10	28.1	
$p \approx 1.7 \times 10^{20}$cm^{-3}	300	0.33±0.03	0.165±0.10	29.5	1.37

Chapter 6

Low Temperature Measurements

6.1 Introduction

Magnetic studies for Pb and Mn-doped SnTe alloys revealed that they exhibit either a paramagnetic or a ferromagnetic phase down to 4 K, depending on the values of the carrier concentration and the concentration of magnetic impurities. As shown in Figure 6.1, materials with carrier concentration less than $\approx 5 \times 10^{20}$ cm^{-3} are paramagnetic, while those with higher carrier concentration are ferromagnetic [3, 42, and 43]. These alloys exhibit spin glass behaviour at very low temperatures [3, 4, and 5], which is also shown in the magnetic phase diagram of Figure 6.1. Samples with a high Mn concentration exhibit a reentrant-spin glass phase, a phase intermediate between ferromagnetic and spin glass, where the spin-glass behaviour does not simply cease but persists into the ferromagnetic phase [5].

A spin glass system can be described as a random distribution of a small amount of magnetic atoms throughout a non-magnetic crystal lattice, with a mixture of ferromagnetic and antiferromagnetic interactions as well as a number of frustrated spins. Figure 6.2 shows a 2D lattice of a non-magnetic metal doped with a number of magnetic impurities. The dots and the arrows represent the lattice sites and the magnetic impurity spins, respectively. The magnetic impurities occupy a certain fraction x of these lattice sites. Assume that the spin pointing up in the right top corner of the figure is the

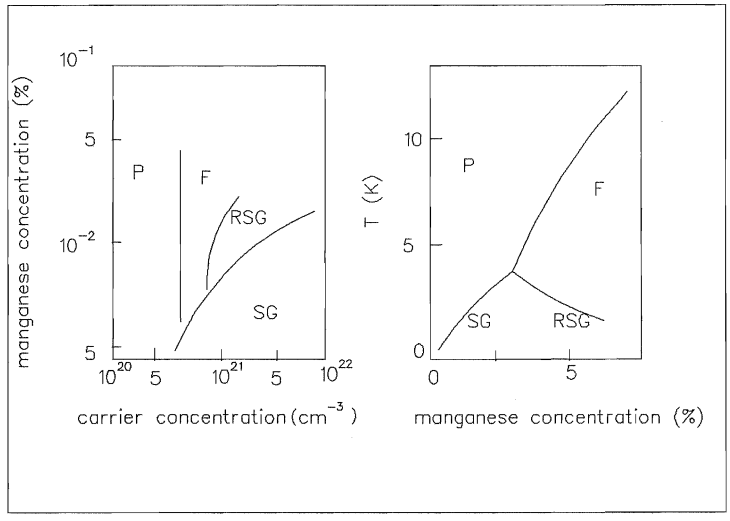

Figure 6.1: The magnetic phase diagram of Pb/Mn-SnTe. P and F refer to a paramagnetic and a ferromagnetic phase, respectively. RSG refers to a reentrant-spin glass phase, an intermediate phase between ferromagnetic and spin glass. SG refers to spin glass phase. This figure is after References [3 and 4].

origin of the lattice, and that the spins have a ferromagnetic ($\uparrow\uparrow$) interaction with the nearest neighbours and an antiferromagnetic ($\uparrow\downarrow$) interaction with the second nearest neighbours. Most of the spins in the lattice will satisfy their first and second nearest neighbours and have a zero net moment. Some of the spins will not be able to satisfy their second neighbours and they will not know in which direction to point. These spins are thus said to be 'frustrated'. The heavy spot in Figure 6.2 indicates such a frustrated spin. It is clear that the frozen spin structure in a 3D lattice will be very complicated [45].

In metallic spin glass materials the most important interaction for coupling the spins is the long-range RKKY interaction. The magnetic impurities cause the susceptibility of the conduction electrons to oscillate in a damped fashion. Thus, depending on the distance between two magnetic ions, the overlapping polarization of the conduction

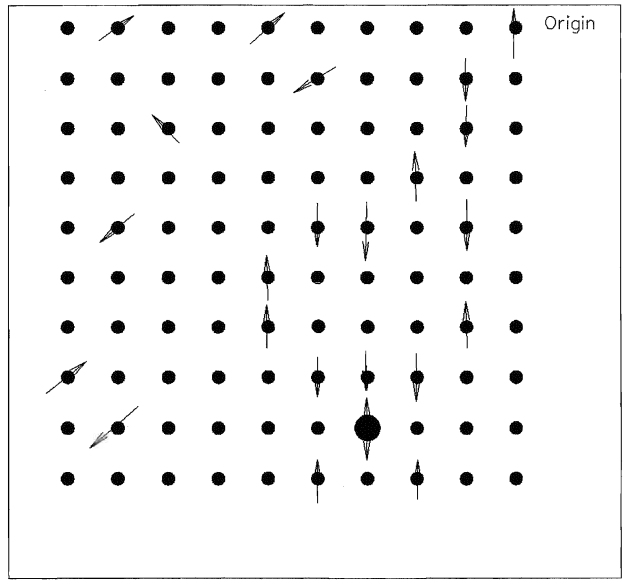

Figure 6.2: Spin glass system. The dots and the arrows represent the lattice sites and the magnetic impurities, respectively. The frustrated spin is indicated by a heavy spot. This figure is adapted from Reference [5].

electrons can induce both ferromagnetic and antiferromagnetic interactions. Insulating and semiconducting materials have few or no conduction electrons, and the coupling of the spins is accomplished by a superexchange interaction. In this case an intervening ligand or anion transfers an electron from one magnetic atom to a neighbouring magnetic atom. This exchange of electrons can lead to both antiferromagnetic and ferromagnetic coupling of the two magnetic ions [5].

The spin glass state is commonly investigated using magnetization, resistivity, specific heat, neutron diffraction and susceptibility measurements. The spin glass susceptibility shows a sharp cusp at the freezing temperature [5, 42, 52 and 53]. Resistivity measurements of spin glass materials [54] find that the impurity resistivity typically exhibits a broad maximum at a temperature T_m significantly higher than the freezing

temperature (T_g), while at T_g the impurity resistivity is observed to vary linearly with temperature.

One of the few optical studies of spin glass materials in the frozen state has been carried out by Cao *et al.* [50]. The reflectance of the spin glass materials, $R_2Mo_2O_{7-\delta}$ (R: Sm, Gd, and Ho), was measured at several temperatures in the spectral range of 40 to 40000 cm^{-1}, and the optical conductivity was obtained by Kramers-Kronig analysis. The optical conductivity of $Sm_2Mo_2O_{7-\delta}$ shows a Drude-like behaviour as the temperature decreases. The scattering rate and the plasma frequency were obtained by fitting the conductivity to the Drude form. The scattering rate shows a monotonic decrease which becomes steeper as the freezing temperature (40 K) is approached due to the increasingly coherent scattering of the conduction electrons by the short-range ordered moments of the magnetic Mo ions. Below 40 K, the scattering rate saturates because the moments are frozen in the spin glass state. The plasma frequency was found to be temperature-dependent with a non-monotonic behaviour that peaked at 150 K and 40 K.

Chernikov *et al.* [53] have studied the spin glass material, $Fe_{1-x}Co_xSi$, with varying x concentration. The dc-conductivity, the specific heat, and the magnetic susceptibility were measured in the temperature range from 0.05 K to 300 K. Susceptibility curves show maxima below 1 K due to the spin glass transition. Reflectance measurements at temperatures ranging from 10 K to 300 K were also carried out on the samples. The optical conductivity and other optical parameters were then obtained using Kramers-Kronig analysis. The optical measurements were however not carried out in the spin glass state.

6.2 Reflectance measurements at low temperature

$Sn_{98}Mn_2Te$ was selected for measurements at very low temperature in the far-infrared, because its moderately low manganese concentration and high carrier concentration make the transition to a spin glass state highly likely. The reflectance of this sample was measured at 69 K, 8 K, and 0.8 K, using a far infrared system comprised of: a Martin-Puplett-type polarizing interferometer, a Helium-3 cryostat, connecting light pipes, and controlling electronics.

The Martin-Puplett interferometer is a modification of the standard Michelson interferometer described in Chapter 2, with polarizing wire grid beam splitter, rooftop mirrors, and a mercury-xenon lamp light-source.

The Helium-3 cryostat provides refrigeration for the sample down to approximately 0.5 K, and houses the bolometer, which is a thermal detector that operates by a change in resistance with temperature. The filtering on the bolometer consisted of rigid white polyethylene with 6 & 15 μm diamond powder. The cryostat had polypropylene windows with one layer of thin black polyethylene on the radiation shield. Further details regarding this system can be found in References [55, 56, and 57].

6.3 Results

The absolute reflectance of the $Sn_{98}Mn_2Te$ sample was determined using a gold-overcoating procedure similar to that described in Chapter 3. The results are shown in Figure 6.3. Note that while the reflectance is very similar at 69 K and 8 K, it becomes noticeably higher at 0.8 K.

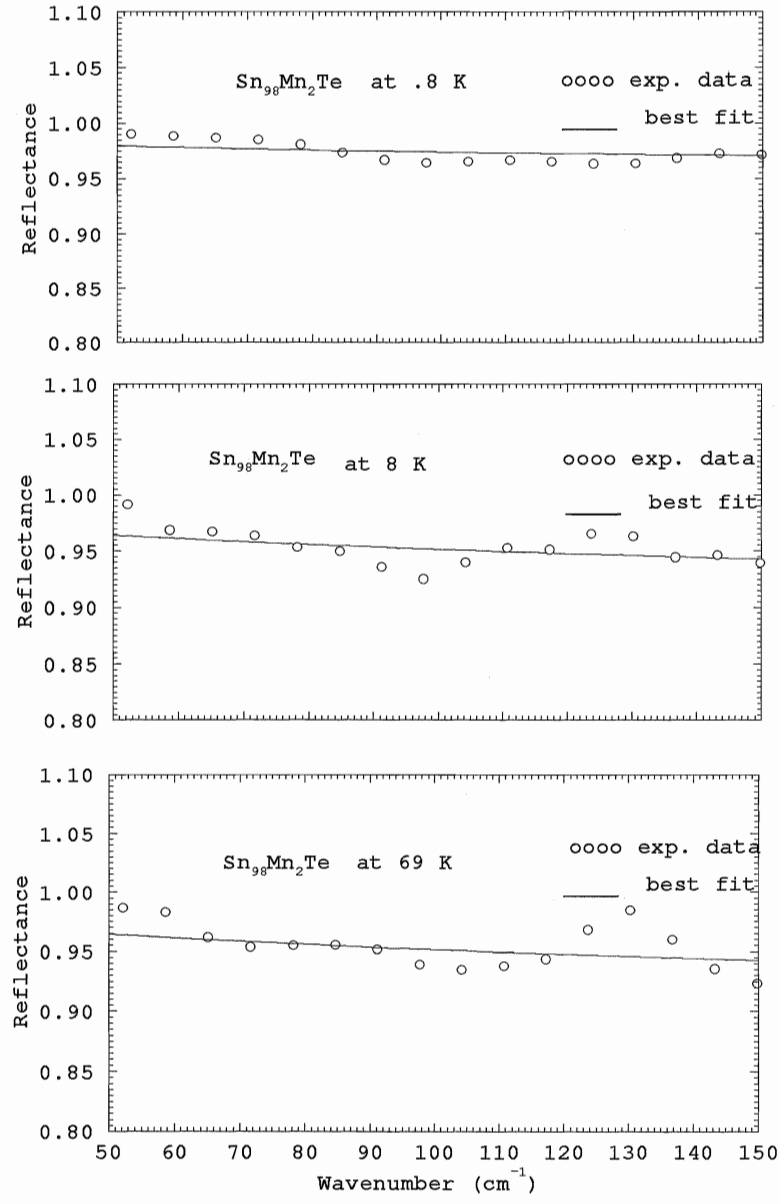

Figure 6.3: The reflectance of $Sn_{98}Mn_2Te$ at several temperatures in the far-infrared. Note the similarity between the 69 K and 8 K curves, and the significant change in the 0.8 K curve.

6.4 Data analysis and discussion

A Drude fit was made to the measured reflectance at each temperature. The fit was carried out by allowing γ to vary, while ω_p was kept constant. A constant value of ϵ_∞ ($\epsilon_\infty = 1$) was used although its value was found to have essentially no effect on the reflectance curve in this spectral region. The best fit to the reflectance curves was done by a computer program and was calculated based on Equations 4.2, 4.10, 4.11, 4.12, 4.30, and 4.31. Table 6.1 shows the γ values found for a particular value of ω_p ($\omega_p = 14000$ cm $^{-1}$). Values of ω_p ranging from 13000 to 15000 cm^{-1} were tried and found to give reasonable fits within the scatter of the data. In each case, however, the temperature dependence of γ exhibited the same trend. In general, the γ values at the three measured temperatures were found to decrease with decreasing temperature. The decrease is more significant in the small temperature range between 8 and 0.8 K, where γ falls by more than a factor of two. Previous studies [4 and 52] showed a decrease in the sample resistivity related to the spin glass transition, which is consistent with the observed decrease in γ. As discussed in the introduction to this chapter the temperature dependence of γ also mirrors that of $Sm_2Mo_2O_{7-\delta}$ as its spin glass freezing temperature is approached [50].

Table 6.1: The temperature dependence of the scattering rate, γ, of $(SnTe)_{98}(MnTe)_2$ obtained from a Drude fit with $\omega_p = 14000$ cm^{-1}.

ω_p (cm^{-1})	T (K)	$\gamma \times 10^{14} s^{-1}$
14000	69	0.21± 0.03
	8	0.19± 0.03
	0.8	0.08 ± 0.03

6.5 Conclusion

The reflectance of $Sn_{98}Mn_2Te$ was measured in the far-infrared at three temperatures which span the spin glass phase transition. Drude fitting revealed a dramatic decrease in the scattering rate between 8 K and 0.8 K, the lowest temperature measured. At this temperature $Sn_{98}Mn_2Te$ is expected to be in the spin glass state and this decrease in γ is consistent with observations in other spin glass systems [50].

Chapter 7

Conclusion

A system comprised of a Bomem interferometer and a cold-finger Helium cryostat was set up to measure the reflectance of single crystal samples in the mid infrared from 500 to 6000 cm^{-1}. Measurements carried out on well studied Silicon and Chromium showed good agreement with the literature [11, 20, and 21], from which it was concluded that this system is capable of producing reliable data and can be used to study materials with less well-known optical properties.

An extended study of SnTe and several Pb and Mn-doped alloys was carried out over the spectral range from 500 to 30000 cm^{-1} at room temperature. Optical conductivity curves are presented for the first time. The fundamental absorption edge was obtained by subtracting the Drude conductivity from the total optical conductivity for each sample. The plasma frequency, ω_p, and the scattering rate, γ, were calculated and found to decrease with decreasing temperature. The optically derived resistivity was essentially constant or tended to decrease with decreasing temperature, in qualitative agreement with the expected metallic nature of these samples. The effective mass at 300 K is found to be 0.17 for SnTe, 0.16 and 0.24 for $(SnTe)_{95}(MnTe)_5$ and $(SnTe)_{98}(MnTe)_2$, respectively, and 1.37 for $[(PbTe)_{75}(SnTe)_{25}]_{95}(MnTe)_5$, which agrees with values reported in References [37, and 38]. The optical parameters presented here take into account the contributions of both free carriers and bound carriers, and therefore are thought to be more accurate than the ones obtained from Drude fits to the reflectance, reported in the

literature, where the contribution of the bound carriers is ignored.

Resistivity measurements at 300 K exhibit the carrier and magnetic concentration dependence expected for Mn-doped SnTe samples. The sample with the lowest carrier concentration (5% Mn) has higher resistivity than the sample with higher carrier concentration (2% Mn). This agrees with the trends reported in References [4, 45, and 51].

Far infrared reflectance measurements were carried out at temperatures as low as 0.8 K on the $Sn_{98}Mn_2Te$ sample, which has a high carrier concentration. The reflectance at 0.8 K is higher compared to that at higher temperatures. The scattering rate, γ, decreases significantly upon decreasing the temperature from 8 to 0.8 K. These observations are interpreted to arise from the spin glass transition reported in References [3, 4, and 42].

Although the mid-infrared system is working well, further improvements such as: extending the spectral range of the measurements, reducing water vapor condensation during low temperature measurements, which affects the quality of the data at these temperatures, and eliminating air absorption by placing the entire system in a purged environment, can be made to ensure the best results.

Appendix A

Transmittance of Optical Windows

A.1 Introduction

The Transmittance measurements of the optical windows were carried out using the Bomem interferometer in transmittance mode, as shown in Figure 2.2. The background (the holder with no sample) was measured first, and then the sample was placed in the sample holder and the transmittance data was collected. The transmittance was calculated as follows [8]:

$$Transmittance = \frac{Sample}{Background} \times 100 \tag{A.1}$$

A.2 The Transmittance of Various Optical Windows

The Transmittance spectra that follow in figures A.1 through A.3 show that KBr has the highest transmittance in the investigated region. Therefore KBr was chosen as an optical window for the mid-infrared reflectance measurements reported herein.

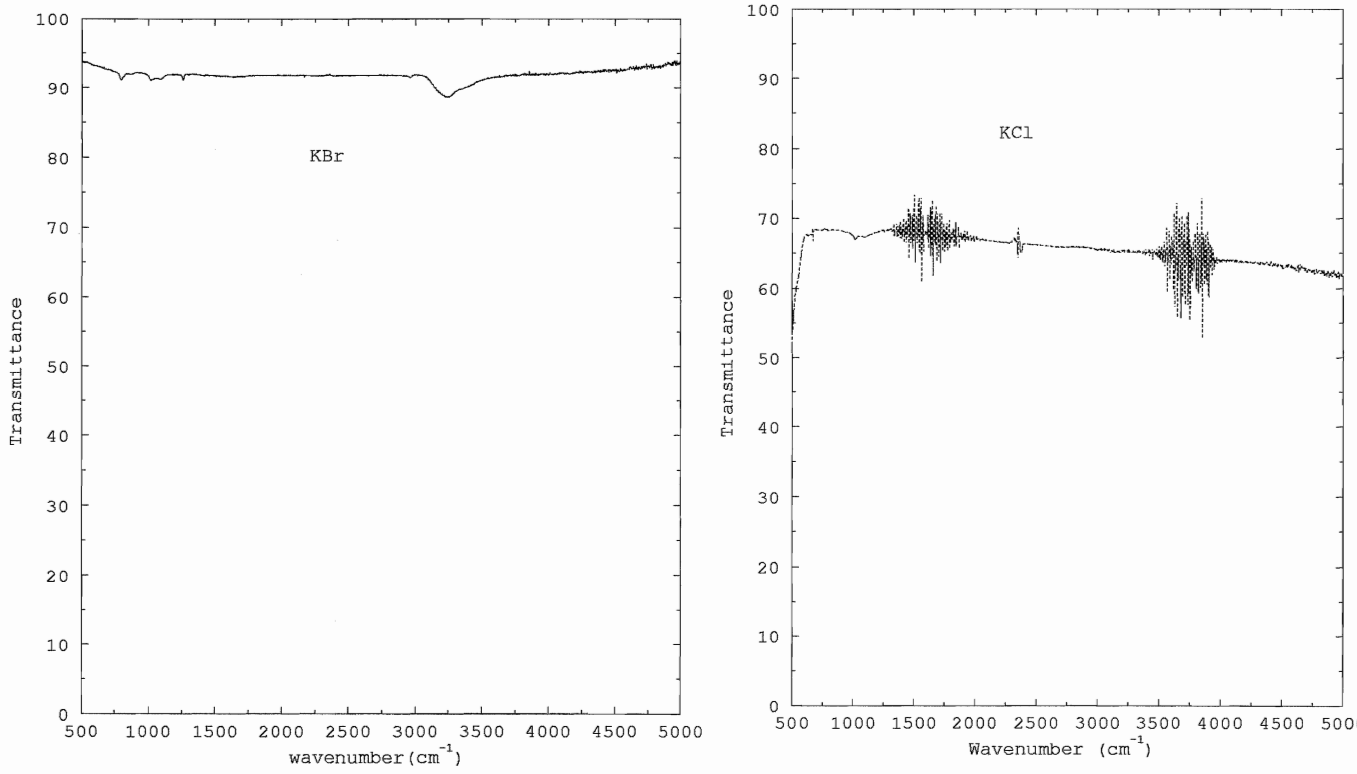

Figure A.1: KBr and KCl Transmittance.

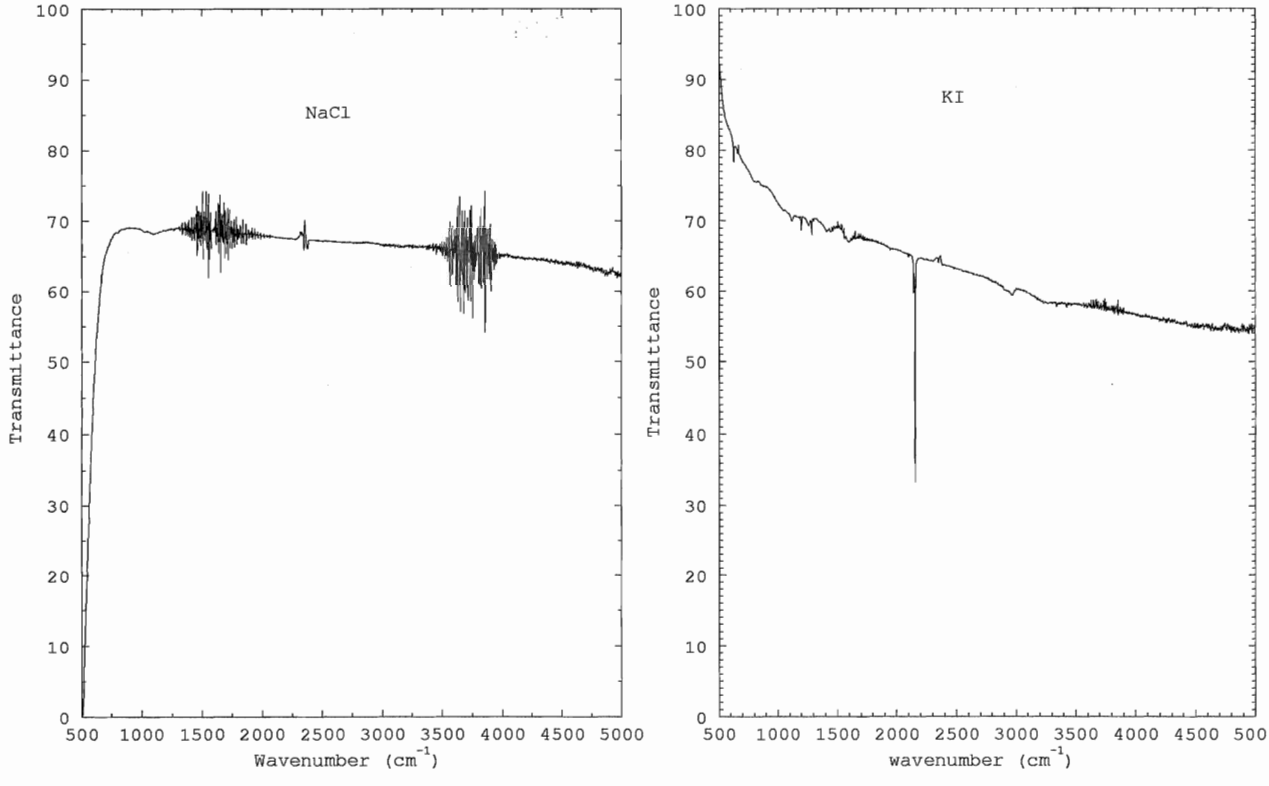

Figure A.2: NaCl an KI Transmittance.

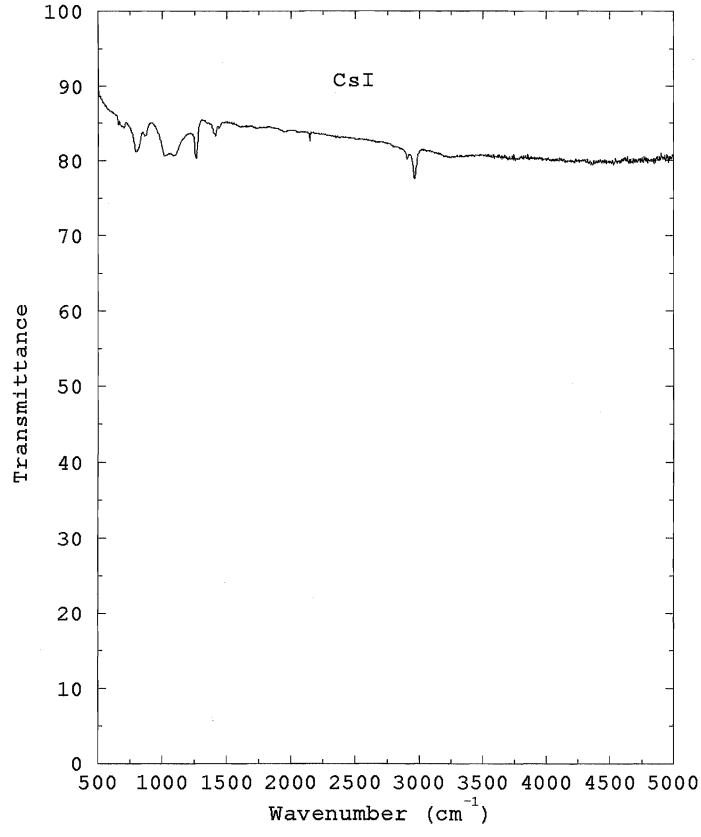

Figure A.3: CsI Transmittance.

Bibliography

[1] Werner Brugel, *Introduction to Infrared Spectroscopy* (Methuen, London, 1962).

[2] James E. Stewart, *Infrared Spectroscopy Experimental Methods and Techniques* (Marce Dekker, INC.,New York, 1970).

[3] P. Eggenkamp and H. Swagten, Phys. Rev. B, Vol. 51, p. 15251, (1995).

[4] M. Escorne and A. Mauger, Phy. Rev. B, Vol. 35, p. 1902, (1987).

[5] J. A. Mydosh, *Spin Glasses: an experimental introduction* (Taylor & Francis, London, 1993).

[6] C. C. Homes, M. Reedyk, D. A. Crandles, and T. Timusk, Applied optics, Vol. 32, p. 2976, (1993).

[7] Liquid Transfer Heli-Tran Refrigeration Operating Manual, The advanced Products Dep., Air Products and Chemical, Inc., Allentown, Pennsylvania 18105.

[8] The Michelson Series User's Guide, Version 1.0, Bomem, inc., Quebec, Canada, (1994).

[9] D. L. Greenaway and G. Harbeke, *Optical Properties and Band Structure Of Semiconductors* (Pergamon Press, Zurich, Switzerland, 1968).

[10] R. Kubo, and T. Nagamiya, *Solid State Physics* (Mcgraw-Hill Book Co., Inc., 1968).

[11] E. D. Palik (Ed.), *Handbook of Optical Constants of Solids*, (Academic Press, San Diego, 1985).

[12] N. W. Ashcroft and N. D. Mermin, *Solid State Physics* (Rinehart and Winston, Philadelphia, 1976).

[13] W. M. Lomer, Proc. Phys. Soc., Vol. 80, p. 489, (1962).

[14] L. W. Bos and D. W. Lynch, Phys. Rev. B, Vol. 2, p. 4567, (1970).

[15] A. W. Overhauser, Phys. Rev., Vol. 128, p. 1437, (1962).

[16] R. S. Hughes and A.W. Lawson, Phys. Letters 25A, p. 473 (1967).

[17] P. A. Fedders and P. C. Martin, Phys. Rev., Vol. 143, p. 245, (1966).

[18] T. M. Rice, A.S. Barker, Jr., B. I. Halperin, and D. B. McWhan, J. Appl. Phys., Vol. 40, p. 1337, (1969).

[19] A. S. Barker and J. A. Ditzenberger, Phys. Rev. Letters, Vol. 20, p. 1164, (1968).

[20] A. S. Barker, Jr., and J. A. Ditzenberger, Phys. Rev. B, Vol. 1, p. 4378, (1970).

[21] E. D Palik(Ed.), *Handbook of Optical Constants of Solids*, Vol. II, (Academic Press, San Diego, 1991).

[22] C. Braun, B.Sc. Thesis, Brock University, 1997.

[23] D. M. Korn and R. Braunstein, Phys. Rev. B, Vol. 5, 4837, (1972).

[24] C. Kittel, *Introduction to Solid State Physics* (John Wiley & Sons, New York, 1986).

[25] Sol Nudelman and S. S. Mitra, *Optical Properties of Solids* (Plenum Press, New York, 1969).

[26] C. A. Wert and R. M. Thomson, *Physics of Solids* (McGraw-Hill Book Company, New York, 1964).

[27] F. Wooten, *Optical Properties of Solids* (Academic Press, New York, 1972).

[28] R. J. Elliott and A. F. Gibson, *An Introduction to Solid State Physics and its Applications* (Barnes and Nobel Books, New York, U.S.A, 1974).

[29] F. Abeles, *Optical Properties of Solids* (North-Holland Publishing Company, London, 1972).

[30] F. Abeles, *Optical Properties and Electronic Structure of Metals and Alloys* (North-Holland Publishing Company, London, 1965).

[31] J. R. Meyer-Arendt, *Introduction to Classical and Modern Optics* (Englewood Cliffs, New Jersey, 1984).

[32] P. F. Robusto and R. Braunstien, Phys. Stat. Sol. (b), Vol. 107, p. 127, (1981).

[33] P. F. Robusto and R. Braunstien, Phys. Stat. Sol. (a), Vol. 119, p. 145, (1990).

[34] H. R. Riedl, J. R. Dixon, and R. B. Schoolar, Phys. Rev., Vol. 162, p. 692, (1967).

[35] V. V. Gorbachev, A. S. Okhotin, V. M. Malovetskaya, and I. M. Putilin, Soviet Physics-Semiconductors, Vol. 6, p. 900, (1972).

[36] R. B. Schoolar and J. R. Dixon, J. of Opt. Society of Amer., Vol. 58, p. 119, (1968).

[37] R. F. Bis and J. R. Dixon, Phys. Rev. B, Vol. 2, p. 1004, (1970).

[38] M. Escorne and A. Mauger, Le Journal De Physics, Vol. 40, p. 347, (1979).

[39] D. M. Korn and R. Braunstien, Phys. Stat. Sol. (b), Vol. 50, p. 77, (1972).

[40] H. R. Riedl, J. R. Dixon and R. B. Schoolar, Solid State Comm.., Vol. 3, p. 323, (1965).

[41] E. G. Bylander, J. R. Dixon, H. R. Riedl, And R. B. Schoolar, Phys. Rev., Vol. 138, p. A864, (1964).

[42] P. J. Eggenkamp, C. M. Vennix, T. Story, and H. J. Swagten, J. Appl. Phys., Vol. 75 , p. 5728 (1994).

[43] T. Story and R. R. Galazka, Phys. Rev. Letters, Vol. 56, p. 777, (1986).

[44] M. Escorne and A. Mauger, Le Journal De Physics, Vol. 40, p. 347, (1979).

[45] M. P. Mathur, D. W. Deis, C. K. Jones, A. Patterson, and W. J. Carr, J. of Appl. Phycs., Vol. 42, p. 1693, (1971).

[46] J. R. Burke and H. R. Riedl, Phys. Rev., Vol. 184, p. 830, (1969).

[47] K. L. I. Kobayashi, Y. Kato, Y. Katayama, and K. F. Komatsubara, Phys. Rev. Letters, Vol. 37, p. 772, (1976).

[48] E. Abramof, S. O. Ferreira, P. H. Rappi, H. Closs and N. Banderia, J. Appl. Phys., Vol. 88, p. 2405, (1997).

[49] Norihiro Suzuki and Sadao Adachi, Jpn. J. Appl. Phys. Vol. 34, p. 5977, (1995).

[50] N. Cao, T. Timusk, N. P. Raju, J. E. Greedan, and P. Gougeon, J. Phys. : Condensed Matter, Vol. 7, p. 2489, (1995).

[51] M. Inoue, H. Yagi, and S. Morishita, J. Phys. Soc. Japan, Vol. 34, p. 562, (1973).

[52] M. Escorne and A. Mauger, Phys. Rev. B, Vol. 29, p. 6306, (1984).

[53] M. Chernikov, L. Degiorgi, E. Felder, S. Paschen, A. Bianchi, and H. R. Ott, J. L. Sarro, Z. Fisk, and D. Mandrus, Phys. Rev. B, Vol. 56, p. 1366, (1997).

[54] A. Mydosh, P. Ford, M. Kawatra, and T. Whall, Phys. Rev. B, Vol. 10, p. 2845 (1974).

[55] Katarin Alinta Baskin, M.Sc. Thesis, Brock University, 1996.

[56] M. Sholtze, B.Sc. Thesis, Brock University (1996).

[57] M. G. Hildebrand, B.Sc. Thesis, Brock University (1997).